The Astrophysical Journal, 1008:142 (20pp), 2026 September 10 https://doi.org/10.3847/1538-4357/ae8b9d
© 2026. The Author(s). Published by the American Astronomical Society.
OPEN ACCESS

# The Open Cluster Chemical Abundances and Mapping Survey. IX. Measuring the Effects of Stellar Diffusion in the Open Clusters NGC 752 and Ruprecht 147 Using APOGEE

Diogo Souto[1], Taylor Spoo[2], Peter M. Frinchaboy[2,3], Katia Cunha[4,5], Jamie Tayar[6], Alessa Ibrahim Wiggins[2], and Natalie Myers[2]

[1] Departamento de Física, Universidade Federal de Sergipe, Av. Marcelo Deda Chagas, S/N Cep 49.107-230, São Cristóvão, SE, Brazil; diogosouto@academico.ufs.br
[2] Department of Physics and Astronomy, Texas Christian University, TCU Box 298840, Fort Worth, TX 76129, USA
[3] Maunakea Spectroscopic Explorer, Canada-France-Hawaii Telescope, Kamuela, HI 96743, USA
[4] Steward Observatory, University of Arizona, 933 North Cherry Avenue, Tucson, AZ 85721-0065, USA
[5] Observatório Nacional/MCTIC, R. Gen. José Cristino, 77, 20921-400, Rio de Janeiro, Brazil
[6] Department of Astronomy, University of Florida, 211 Bryant Space Science Center, Gainesville, FL 32611, USA
*Received 2025 October 30; revised 2026 July 14; accepted 2026 July 14; published 2026 September 1*

## Abstract

A growing understanding of stellar processes that alter surface chemical abundances over time has opened new avenues for using these changes as probes of stellar properties. On the main sequence and near the turnoff, stellar surface abundances are affected by gravitational settling and radiative acceleration, collectively known as atomic diffusion. In this work, we use Sloan Digital Sky Survey/APOGEE DR17/DR19 data to investigate atomic diffusion in the open clusters NGC 752 and Ruprecht 147, thereby constraining how these signatures vary with age. From the analysis of Fe, C, N, Na, Mg, Al, Si, S, K, Ca, Ti, V, Cr, Mn, Co, and Ni, we find significant abundance differences between stars near the turnoff and the cooler main sequence, where warmer stars are depleted relative to the cooler main-sequence stars at the $\geqslant 1\sigma$ level for all elements available in the analysis. These abundance differences are consistent with the signatures expected from atomic diffusion and are further supported by comparisons with stellar models that include diffusion. By fitting the observed $T_{\rm eff}$–[Fe/H] patterns with MIST isochrones, we obtain best-fit ages of 1.0 Gyr for NGC 752 and 2.5–3.2 Gyr for Ruprecht 147. Carbon is a key diagnostic, as it shows both atomic diffusion and extra-mixing signatures associated with first dredge-up. For NGC 752, the coolest stars in our sample, which provide the best proxy for the initial cluster composition, yield $[{\rm Fe/H}]_{\rm CS} = 0.01 \pm 0.02(\pm 0.05)$ dex. For Ruprecht 147, we obtain $[{\rm Fe/H}]_{\rm CS} = 0.17 \pm 0.00(\pm 0.05)$ dex. Our findings further constrain atomic diffusion models, suggesting that atomic diffusion affects age estimates of stars near the main-sequence turnoff.

*Unified Astronomy Thesaurus concepts:* Open star clusters (1160); Galactic abundances (2002); Chemical abundances (224); Abundance ratios (11)

*Materials only available in the online version of record: figure set, machine-readable table*

## 1. Introduction

Precise measurements of stellar abundances and ages are fundamental tools in Galactic archeology, allowing us to reconstruct the formation and evolutionary history of the Milky Way from the fossil record preserved in its stars (K. Freeman & J. Bland-Hawthorn 2002). Open clusters are especially valuable for these studies, as their well-constrained ages, distances, and compositions offer critical benchmarks for calibrating stellar models and probing chemical evolution across the Galactic disk (S. Randich et al. 2018; L. Magrini et al. 2023). However, accurately interpreting observed abundance patterns requires accounting for stellar processes such as atomic diffusion and internal mixing, which can significantly modify surface compositions and introduce systematic biases into abundance-derived ages if neglected (J. Choi et al. 2016; A. Dotter 2016; A. Dotter et al. 2017).

A widely adopted approach for determining stellar ages involves modeling the evolution of luminosity and effective temperature with time to construct theoretical isochrones, which describe stellar populations at specific ages. By matching observed stars to isochrones with the corresponding chemical compositions, precise age estimates can be obtained. Stars near the main-sequence turnoff (MSTO) and along the subgiant branch (SGB) are particularly suitable for this technique, typically yielding ages with uncertainties of ~10%–20% under favorable observational conditions (e.g., D. R. Soderblom 2010; L. Casagrande et al. 2016). Recent large-scale spectroscopic surveys, such as the Apache Point Observatory Galactic Evolution Experiment (APOGEE; Abdurro'uf et al. 2022), the Gaia-ESO Survey (G. Gilmore et al. 2012), and the GALactic Archeology with HERMES survey (GALAH; S. L. Martell et al. 2017), have substantially enhanced the applicability of this method. Combined with Gaia astrometry, these surveys enable robust studies of stellar ages throughout the Galaxy, particularly through targeted observations of SGB stars (e.g., M. R. Hayden et al. 2022; M. Xiang & H.-W. Rix 2022).

However, standard isochrone fitting typically assumes that a star's observed surface abundances reflect its initial, birth

Original content from this work may be used under the terms of the Creative Commons Attribution 4.0 licence. Any further distribution of this work must maintain attribution to the author(s) and the title of the work, journal citation and DOI.

composition. In practice, this assumption breaks down owing to various internal mixing processes that alter the surface chemical composition over time. Stars are dynamic systems, and material can be exchanged between the stellar interior and atmosphere through both convective and nonconvective processes. For example, in red giants, it is well established that the first dredge-up (FDU) modifies the surface abundances of carbon and nitrogen, a convective episode that transports material processed via the CNO cycle from the interior to the surface (N. Lagarde et al. 2012; A. I. Karakas & J. C. Lattanzio 2014). Atomic diffusion is another well-established physical process that operates more efficiently in stars near the MSTO and, to a lesser degree, along the SGB. First proposed over a century ago (S. Chapman 1917a, 1917b), atomic diffusion arises from the interplay of gravitational settling, which causes heavier elements to sink below the surface, and radiative levitation, which can counteract this effect by pushing certain ions upward. As a result, surface photospheric abundances gradually diverge from the star's pristine composition. In particular, elements may diffuse out of the convective envelope, leading to surface depletions that persist until mixing processes restore them. During red giant evolution, the deepening of the convective envelope can dredge up material from the interior, reestablishing surface abundances that more closely reflect the stellar interior (G. Michaud et al. 2004). Atomic diffusion is expected to be most effective in the outer layers of main-sequence stars with effective temperatures above 6000 K and in horizontal branch stars with $T_{\rm eff} > 8000$ K (J. Richer et al. 1998; A. Dotter et al. 2017).

Fortunately, atomic diffusion has been extensively studied both theoretically and observationally (G. Michaud et al. 2015, and references therein). Clear signatures of this process have been detected in several globular clusters, including M92 (A. M. Boesgaard et al. 1998; J. R. King et al. 1998), NGC 6397 (A. J. Korn et al. 2006, 2007), and NGC 6752 (P. Gruyters et al. 2013, 2014). More recently, evidence for atomic diffusion has also been reported in M4 (T. Nordlander et al. 2024), as well as in a number of open clusters, such as M67 (A. Önehag et al. 2014; C. Bertelli Motta et al. 2018; X. Gao et al. 2018; D. Souto et al. 2018a, 2019; F. Liu et al. 2019), NGC 2420 (E. Semenova et al. 2020), and Coma Berenices (D. Souto et al. 2021). V. Grilo et al. (2024) investigated potential signatures of atomic diffusion in the young open cluster Pleiades (age ∼100 Myr) but found no statistically significant evidence for diffusion-related abundance variations. Star clusters provide ideal laboratories for studying atomic diffusion, as they contain stars at various evolutionary stages with shared ages and compositions. By comparing abundance patterns across the main-sequence, turnoff, and red giant phases, we can assess the signatures of atomic diffusion and evaluate its implications for stellar evolution.

In this study, we investigate the signatures of atomic diffusion across multiple elements from abundances derived using spectra from the Sloan Digital Sky Survey (SDSS)/APOGEE survey. This work builds on D. Souto et al. (2018a, 2019), employing a similar methodology that includes the use of consistent isochrone models and detailed spectroscopic abundance determinations, as well as the APOGEE/ASPCAP (A. E. García Pérez et al. 2016) abundances. Using data from SDSS/APOGEE and applying quality and membership selections based on the OCCAM survey, we expand the analysis to two additional open clusters: NGC 752 and Ruprecht 147. NGC 752 is a nearby (∼450 pc), intermediate-age open cluster with an estimated age of 1.3 Gyr (T. Cantat-Gaudin et al. 2020) and solar metallicity ([Fe/H] $\sim -0.01$ dex; A. B. S. Reddy et al. 2012; R. Carrera et al. 2019; M. G. Lum & A. M. Boesgaard 2019). Ruprecht 147 (also known as NGC 6774) is a middle-aged open cluster (∼2.5 Gyr; T. Cantat-Gaudin et al. 2020) located even closer to the Sun (∼250–300 pc) and has a slightly supersolar metallicity of [Fe/H] $\sim$ 0.10 dex (A. Bragaglia et al. 2018; K. L. Beeson et al. 2024). The proximity and well-characterized properties of these clusters make them ideal targets for precise spectroscopic analysis, enabling us to further explore the impact of atomic diffusion.

## 2. Data and Models

### 2.1. SDSS/APOGEE Survey

In this work, we use data from the Apache Point Observatory Galactic Evolution Experiment surveys (S. R. Majewski et al. 2017, APOGEE-1 and APOGEE-2), which are part of the SDSS-III and SDSS-IV projects (D. J. Eisenstein et al. 2011; M. R. Blanton et al. 2017). Spectroscopic data were obtained in both hemispheres with 2.5 m telescopes (I. S. Bowen & A. H. J. Vaughan 1973; J. E. Gunn et al. 2006) at Apache Point Observatory (APO; New Mexico, USA) and Las Campanas Observatory (LCO; La Serena, Chile), using the APOGEE-N and APOGEE-S spectrographs (J. C. Wilson et al. 2019), respectively. The targeting selection for APOGEE is described in G. Zasowski et al. (2013, 2017), R. L. Beaton et al. (2021), and F. A. Santana et al. (2021), with targeting for open clusters being further described in P. M. Frinchaboy et al. (2013) and J. Donor et al. (2018).

### 2.2. MIST Stellar Evolution Models

To investigate the significance of any diffusion effects, we need to compare the observed data with stellar evolution models. In this work, we have selected the MESA Isochrones & Stellar Tracks (MIST; J. Choi et al. 2016; A. Dotter 2016) models that utilize the stellar evolution code Modules for Experiments in Stellar Astrophysics (MESA; B. Paxton et al. 2011, 2013, 2015), which also includes the effects of atomic diffusion. These models cover an age range of $5 \leqslant \log(\mathrm{Age}) \leqslant 10.3$ and a metallicity range of $-4 \leqslant [\mathrm{Fe/H}] \leqslant +0.5$ and report surface abundances for 19 isotopes of 17 elements from hydrogen to iron. Stellar evolutionary tracks were computed with and without radiative acceleration to gauge their influence. Each element is treated independently in the calculation of ionization balance, monochromatic opacity, and radiative acceleration. For elements without explicit atomic diffusion evolution in the isochrones, we adopt the iron abundance as a proxy. All isochrones used in this study were generated using the MIST Isochrone Interpolation tool.[7]

## 3. Analysis

Our stellar data are taken from the first data release of the SDSS-V Milky Way Mapper (MWM) survey (DR19; SDSS Collaboration et al. 2026b). A full description of the APOGEE data quality and parameter limitations is presented in Abdurro'uf et al. (2022). For this work, we have selected the

[7] https://waps.cfa.harvard.edu/MIST/interp_isos.html

SDSS/APOGEE survey to study diffusion in the open clusters NGC 752 and Ruprecht 147. These open clusters were selected because they cover a wide range in stellar class from dwarfs to red giant stars. Notably, besides the open cluster M67 that was previously studied in D. Souto et al. (2018a, 2019), NGC 752 and Ruprecht 147 are the only clusters in the OCCAM sample that include stars spanning the main-sequence, turnoff, and red giant branch (RGB) evolutionary stages. This full evolutionary coverage is essential for probing abundance variations near the turnoff, where atomic diffusion signatures are expected to be most prominent.

### 3.1. Cluster Membership and Selected Sample

To select open-cluster members for this study, we used the cluster membership probabilities from the Open Cluster Chemical Analysis and Mapping (OCCAM) survey (P. M. Frinchaboy et al. 2013; K. Cunha et al. 2015; J. Donor et al. 2018, 2020; N. Myers et al. 2022; J. M. Otto et al. 2026). Specifically, we used the OCCAM proper-motion (PM) and radial velocity (RV) membership probabilities from the N. Myers et al. (2022) Value Added Catalog (VAC) to select members of NGC 752 and Ruprecht 147. We adopted a cutoff RV PROB $> 0.1$ and RV PROB $> 0.1$. We checked that the same sample is obtained when using the J. M. Otto et al. (2026) DR19 results. We note that we did not use the metallicity-based probability, as it could remove stars with potential signatures for atomic diffusion, since the iron surface abundance would change at and around the turnoff phase.

We also used RV measurements from different APOGEE observations of the same star to remove possible binaries from our sample. The DR17 parameter VSCATTER provides the scatter around the average RV determined from individual stellar visits; here we applied a VSCATTER cut of $<1\ \mathrm{km\ s^{-1}}$. In addition, we selected only stars with reliable stellar parameters and elemental abundance measurements in DR17 by applying the APOGEE/ASPCAP quality bit-wise flags described in H. Jönsson et al. (2020). Specifically, we excluded stars flagged by the relevant DR17 stellar-parameter STARFLAG criterion and by the ASPCAP chemistry-quality flag, corresponding to the STARFLAG and ASPCAP flag cuts previously summarized as STARFLAG $\neq 16$ and ASPCAP chemistry flag $\neq 23$. We further required APOGEE spectra with signal-to-noise ratio (SNR) $\geqslant$100. To ensure cluster membership, we adopted the OCCAM survey VAC probabilities from N. Myers et al. (2022), requiring both RV membership probability RV_PROB $> 0.1$ and PM membership probability PM_PROB $> 0.1$. After applying these selection criteria, our final sample consists of 35 stars from NGC 752 and 23 stars from Ruprecht 147.

Figure 1 presents the photometric and spectroscopic properties of our final sample in NGC 752 and Ruprecht 147. The left panels show the dereddened color–magnitude diagrams (CMDs), $M_{K_s}$ versus $(J-K_s)_0$, while the right panels show a narrow APOGEE $H$-band spectral region containing three strong Mg I features. The top and bottom rows correspond to NGC 752 and Ruprecht 147, respectively. In the CMD panels, we overplot the adopted MIST isochrone for each cluster as a solid gray curve, together with two additional isochrones offset by $\pm 0.3$ Gyr from the adopted cluster age, shown as dashed gray curves. The symbols indicate the evolutionary classes adopted in this work, as defined in Section 4.1: cool stars (CS), main-sequence stars (MS), diffusion-dominated stars (Diff), main-sequence–turnoff transition stars (MS–TO), and red giants (RG). The spectroscopic panels show the observed APOGEE spectra for stars in each of these evolutionary classes, ordered from evolved stars at the top to cooler main-sequence stars at the bottom. The shaded regions mark the Mg I features highlighted in this figure and illustrate how the line strengths vary across the cluster sequences. The stellar parameters and abundances for the full sample are listed in Table 1.

### 3.2. Atmospheric Parameters: $T_{eff}$ and log g

We determined the effective temperatures for the studied stars using the color–$T_{\rm eff}$ relations of J. I. González Hernández & P. Bonifacio (2009), adopting the calibrations appropriate for dwarf and giant stars. For each star, we computed temperatures from five color indices: $B-V$, $V-J$, $V-H$, $V-K_s$, and $J-K_s$. The optical $B$ and $V$ magnitudes were taken from the UCAC4 catalog (N. Zacharias et al. 2013), and the near-infrared $J$, $H$, and $K_s$ magnitudes were taken from the Two Micron All Sky Survey (2MASS; R. M. Cutri et al. 2003). We adopted cluster metallicities of [Fe/H] $= -0.04$ dex for NGC 752 and [Fe/H] $= +0.12$ dex for Ruprecht 147 when applying the calibrations. The final photometric $T_{\rm eff}$ was defined as the mean value obtained from the five color indices, and the dispersion among the individual color temperatures is used as an estimate of the internal uncertainties. A detailed comparison of $T_{\rm eff}$ from this work with those from APOGEE/ASPCAP DR17 and DR19 is presented in Appendix A.

We determined surface gravities using Equation (1), which follows directly from the Stefan–Boltzmann law combined with the definition of surface gravity,

$$\log g = \log g_{\odot} + \log\left(\frac{M}{M_{\odot}}\right) + 4\log\left(\frac{T_{\rm eff}}{T_{\rm eff,\odot}}\right) - \log\left(\frac{L}{L_{\odot}}\right). \quad (1)$$

For each star, we adopted the photometric $T_{\rm eff}$ values determined in this work, together with stellar masses and luminosities estimated from MIST isochrones appropriate for each cluster. We assumed an age of 1.3 Gyr and [Fe/H] $= -0.04$ dex for NGC 752 and an age of 2.5 Gyr and [Fe/H] $= +0.12$ dex for Ruprecht 147, following T. Cantat-Gaudin et al. (2020) ages and metallicities from A. B. S. Reddy et al. (2012), M. G. Lum & A. M. Boesgaard (2019), R. Carrera et al. (2019), A. Bragaglia et al. (2018), and K. L. Beeson et al. (2024). Stellar masses and luminosities were assigned by comparing each star with the corresponding isochrone, using the adopted $T_{\rm eff}$ and the $K_s$ magnitude as reference quantities, and selecting the closest matching point along the isochrone. We adopted the solar reference values of $\log g_{\odot} = 4.438$ dex and $T_{\rm eff,\odot} = 5772$ K, following the IAU recommendations of A. Prša et al. (2016).

### 3.3. Detailed Abundance Analysis

In this study, we performed a detailed spectroscopic analysis to determine chemical abundances for all stars in our sample using the effective temperatures and surface gravity values discussed in the previous section. These detailed abundance determinations provide an independent benchmark against which we compare the automated results from the ASPCAP pipeline, as presented in Appendix B.

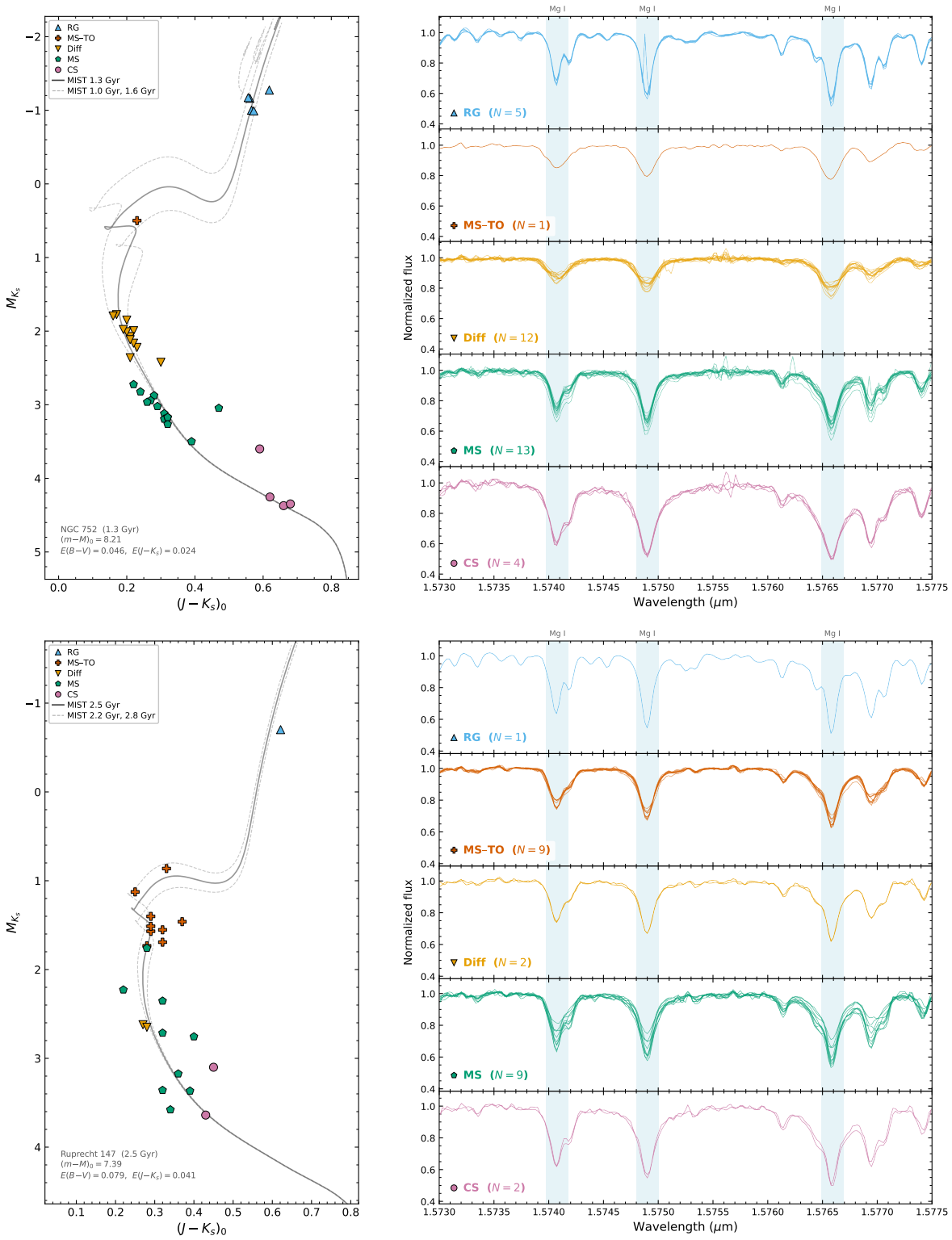


**Figure 1.** CMD and APOGEE spectra for stars in NGC 752 and Ruprecht 147 in the top and bottom panels, respectively. The left panel shows the dereddened $M_{K_s}$ vs. $(J - K_s)_0$ diagram. Symbols indicate the evolutionary classes adopted in this work: red giants (RG; blue triangles), main-sequence–turnoff transition stars (MS–TO; orange plus signs), diffusion-dominated stars (Diff; yellow inverted triangles), main-sequence stars (MS; green pentagons), and cool stars (CS; pink circles). The solid gray curve shows the MIST isochrone for the adopted cluster parameters, and dashed gray curves show MIST isochrones with ages ±0.3 Gyr for comparison. The right panels show the normalized APOGEE spectra in the wavelength interval 1.5730–1.5775 $\mu$m, separated by evolutionary class. Individual stellar spectra are shown as thin colored curves, and the number of stars in each group is indicated in each panel. The light-blue shaded regions mark the Mg I features used to illustrate the spectral behavior across the cluster sequence.

The spectral analysis was carried out using the BACCHUS code (T. Masseron et al. 2016), with MARCS models of atmosphere (B. Gustafsson et al. 2008), and we derive elemental abundances by fitting synthetic spectra to observed lines via a minimum $\chi^2$ criterion with further visual inspection. For estimating the microturbulence velocity, we adopted the

**Table 1**
Stellar Parameters and Elemental Abundances

| SDSS_ID | Cluster | $J_0$ | $H_0$ | $K_0$ | S/N | Phase | $M/M_\odot$ | $T_{\rm eff}$ | log $g$ | [Fe/H] | … |
|---|---|---|---|---|---|---|---|---|---|---|---|
| 116885323 | NGC 752 | 10.607 | 10.442 | 10.379 | 183.3 | Diff | 1.28 | 6678 | 4.30 | −0.044 | … |
| 116885668 | NGC 752 | 7.581 | 7.141 | 7.024 | 414.4 | RG | 1.87 | 4982 | 2.99 | −0.030 | … |
| 116885332 | NGC 752 | 10.937 | 10.696 | 10.640 | 154.9 | Diff | 1.24 | 6385 | 4.29 | −0.063 | … |
| 116886272 | NGC 752 | 10.263 | 10.109 | 10.063 | 305.7 | Diff | 1.28 | 6719 | 4.31 | −0.112 | … |
| 116886106 | NGC 752 | 11.457 | 11.212 | 11.168 | 191.7 | MS | 1.14 | 6190 | 4.38 | 0.034 | … |
| … | … | … | … | … | … | … | … | … | … | … | … |

**Note.** The full machine-readable table contains the SDSS identifier; cluster name; dereddened 2MASS photometry ($J_0$, $H_0$, and $K_0$); APOGEE SNR; evolutionary phase; isochrone-derived stellar mass; $T_{\rm eff}$; log $g$; the abundance ratios [Fe/H], [C/H], [N/H], [Na/H], [Mg/H], [Al/H], [Si/H], [S/H], [K/H], [Ca/H], [Ti/H], [V/H], [Cr/H], [Mn/H], [Co/H], and [Ni/H]; the corresponding abundance uncertainties e_[C/H], e_[N/H], e_[Na/H], e_[Mg/H], e_[Al/H], e_[Si/H], e_[S/H], e_[K/H], e_[Ca/H], e_[Ti/H], e_[V/H], e_[Cr/H], e_[Mn/H], e_[Fe/H], e_[Co/H], and e_[Ni/H]; the Gaia DR3 source identifier; and the SDSS-IV APOGEE identifier. Ellipses indicate measurements that could not be reliably determined for a given star.

(This table is available in its entirety in machine-readable form in the online article.)

same procedure as in D. Souto et al. (2016) and V. V. Smith et al. (2013), and the same spectral lines as in D. Souto et al. (2018a) were analyzed to determine individual abundances of the elements: C, N, Na, Mg, Al, Si, S, K, Ca, Ti, V, Cr, Mn, Fe, Co, and Ni. It is important to note that for specific elements, such as Ti, V, Cr, and Co, the neutral atomic lines become quite weak as the effective temperature increases. This is the case, in particular, for turnoff stars, for which the determination of precise individual abundances becomes more challenging or impossible. The chemical abundances obtained from our detailed analysis are presented in Table 1.

The estimated abundance uncertainties here are the same as those reported in Table 4 of D. Souto et al. (2018a), as our analysis methodology and atmospheric parameter range for the sample are very similar. The abundances of Fe consistently exhibit the lowest total uncertainties (typically $<$0.07 dex) across all evolutionary stages (main sequence, turnoff, and red giants), making it a robust indicator for comparative chemical studies. The abundances of carbon and calcium also display relatively small uncertainties, below 0.07 dex in most cases, although the uncertainties are slightly higher for red giants. In contrast, silicon and magnesium abundances show increased sensitivities, particularly to effective temperature and microturbulent velocity, resulting in abundance uncertainties up to $\sim$0.10 dex for turnoff stars.

The mean open-cluster Fe abundances and standard deviations obtained from our detailed analysis are $\langle$[Fe/H]$\rangle$ $-0.03 \pm 0.04$ for NGC 752 and $\langle$[Fe/H]$\rangle = 0.14 \pm 0.04$ for Ruprecht 147. These mean Fe abundances and their associated dispersions are slightly larger than the level of chemical homogeneity reported by A. Sinha et al. (2024), who found that most open clusters exhibit internal abundance scatters of $\leqslant$0.02 dex across well-measured elements. Although NGC 752 and Ruprecht 147 were not part of their cluster sample, our slightly larger internal dispersions (0.04 dex) may reflect subtle abundance variations driven by physical processes such as atomic diffusion, particularly given our deliberate selection of stars across a range of evolutionary stages, which we discuss in detail in the next section.

### 3.4. Deviation from the Local Thermodynamical Equilibrium

Based on the previous non–local thermodynamical equilibrium (NLTE) study in the APOGEE $H$ band by Y. Osorio et al. (2020), we do not expect large NLTE abundance corrections for the stars analyzed in this work. For Na, K, and Ca, LTE and NLTE line profiles yield essentially the same abundances in the solar spectrum, while only small differences are found for Ca in Arcturus. Magnesium is the element most affected by NLTE effects, particularly for the strong Mg I lines near 15740–15766 Å, for which line-core differences can become important at APOGEE-like resolution. However, these strong Mg features are excluded from our analysis; instead, we use weaker Mg I lines that are less affected by the reported NLTE departures, as discussed in Section 4.2.4.

## 4. Results and Discussion

This work presents atmospheric parameters and abundance results for 58 stars at different evolutionary stages in the NGC 752 and Ruprecht 147 open clusters. The studied elements are Fe, C, N, Na, Mg, Al, Si, S, K, Ca, Ti, V, Cr, Mn, Co, and Ni. Our sample is designed to probe abundance trends linked to physical processes operating in stars, such as atomic diffusion and extra mixing, as a signature of the FDU. To evaluate the extent of these signatures in the chemical abundances measured for our open-cluster samples, we compare our derived elemental abundances with results and predictions from MIST stellar evolution models. In Appendices A and B, we present a comparison of atmospheric parameters and individual abundances using the APOGEE/ASPCAP pipeline, placing this work's detailed results in context with those derived from automatic pipelines.

### 4.1. Populations as a Function of Stellar Mass

The interpretation of abundance trends along a cluster sequence depends critically on the evolutionary status assigned to each star. Evolutionary classes are traditionally defined from the position of each star in the observed $T_{\rm eff}$–log $g$ plane, or equivalently in the CMD. The atomic diffusion observational signature, which this work aims to seek, is controlled not by the evolutionary label itself but by the structure of the star. The abundance surface depletion produced by diffusion depends primarily on the mass of the surface convection zone and on the additional mixing processes that counteract gravitational settling (A. A. Thoul et al. 1994; A. Dotter et al. 2017), both of which are functions of stellar mass. At a fixed near-solar composition and an age typical of open clusters (0.6–3.0 Gyr), the maximum depletion occurs at an approximately age-independent mass of $M_\star \simeq 1.25\,M_\odot$, whereas the cluster turnoff mass decreases with age. Therefore, depending on the

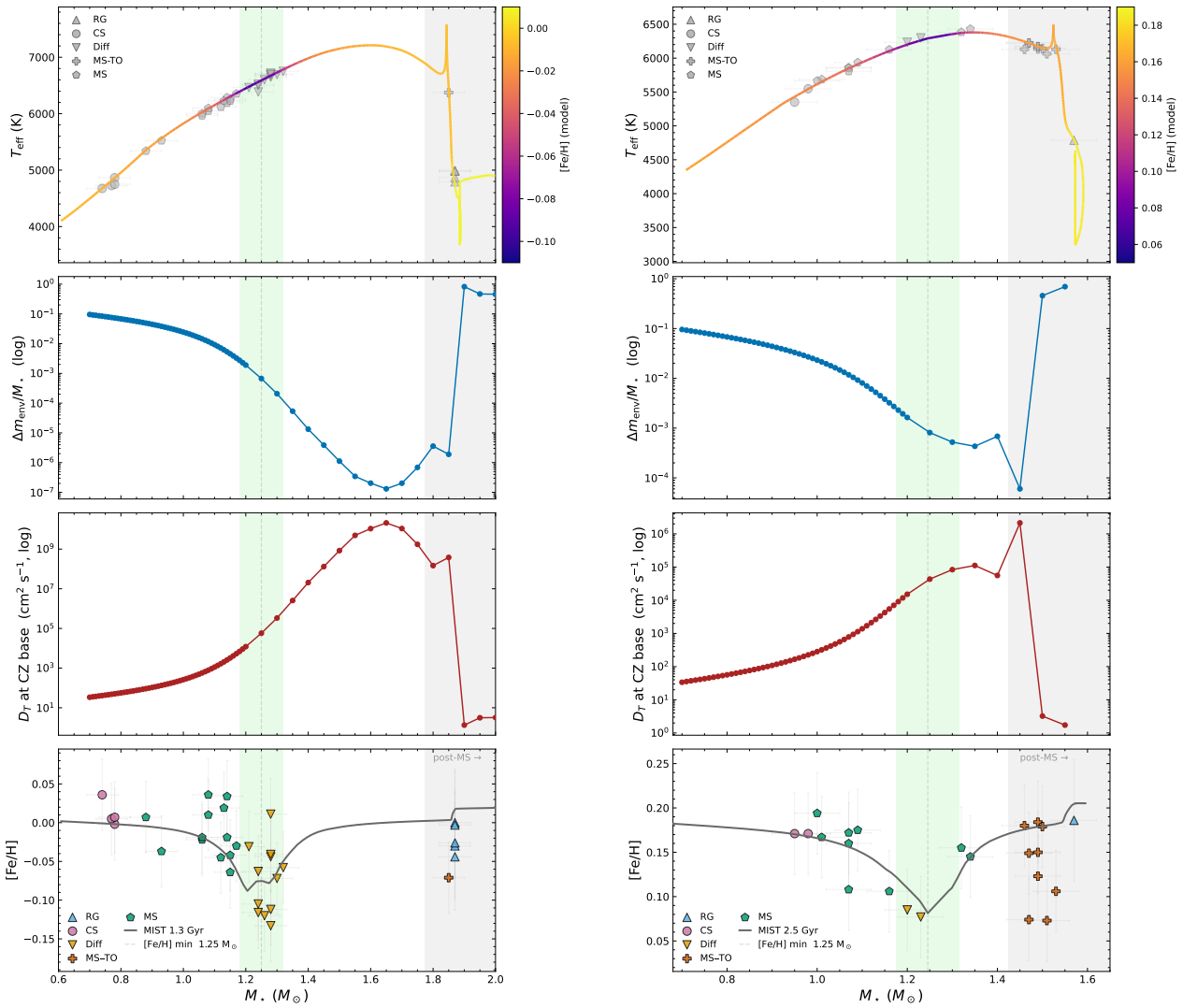


**Figure 2.** Atomic diffusion diagnostics as a function of stellar mass for NGC 752 (left) and Ruprecht 147 (right). In each column, the four panels share the same abscissa (isochrone-derived stellar mass); the green band marks the predicted [Fe/H] minimum ($M_\star = 1.25 \pm 0.05\,M_\odot$ for NGC 752), and the gray region marks masses evolved past the main sequence at the cluster age. First panel: mass–$T_{\rm eff}$ plane; the solid curve is the MIST isochrone (1.3 Gyr for NGC 752; 2.5 Gyr for Ruprecht 147), color coded by the model surface [Fe/H], with observed members shown in gray, coded by evolutionary class. Second panel: fractional mass of the surface convection zone from MIST tracks interpolated at the cluster age. Third panel: turbulent-diffusion coefficient $D_T$ evaluated at the base of the convection zone. Fourth panel: observed [Fe/H] vs. stellar mass, coded by evolutionary class, compared with the MIST prediction (solid gray curve).

cluster age, the stars carrying the strongest diffusion signal may be genuine turnoff stars, as in M67 (D. Souto et al. 2018a; F. Liu et al. 2019), or they may be upper-main-sequence stars located well below the turnoff, as in Coma Berenices (D. Souto et al. 2021). Because this distinction determines how the abundance trends in this work should be interpreted, we begin by discussing the mass domain and use it to define the evolutionary classes adopted throughout the remainder of the paper.

Figure 2 presents the mass-based diagnostics for NGC 752 (left) and Ruprecht 147 (right). In each column, four vertically stacked panels share a common abscissa, the isochrone-derived stellar mass. From top to bottom, the panels show (i) the mass–$T_{\rm eff}$ plane, with the MIST isochrone (J. Choi et al. 2016; A. Dotter et al. 2017) color coded by the model surface [Fe/H] at each point along the sequence; (ii) the fractional mass of the surface convection zone, $\Delta m_{\rm env}/M_\star$, obtained from MIST evolutionary tracks of fixed mass and interpolated to the cluster age (1.3 Gyr for NGC 752 and 2.5 Gyr for Ruprecht 147; T. Cantat-Gaudin et al. 2020); (iii) the turbulent-diffusion coefficient, $D_T$, adopted in the MIST models (Equation (2)); and (iv) the observed [Fe/H] as a function of stellar mass, compared with the model prediction. In all panels, the green shaded band marks the mass range of maximum predicted depletion ($M_\star = 1.25 \pm 0.05\,M_\odot$ for NGC 752; $M_\star \simeq 1.2$–$1.25\,M_\odot$ for Ruprecht 147), while the gray shaded region marks masses that have already evolved off the main sequence at the cluster age.

The two middle panels identify the structural origin of the atomic diffusion depletion signal. The fractional convective envelope mass, shown in the second panel, decreases monotonically by roughly four to six orders of magnitude between $\sim$0.7 and $\sim$1.65 $M_\odot$. A thinner convective envelope contains less mass over which gravitationally settled material can be diluted; therefore, for a similar settling flux, the surface-abundance depletion increases with stellar mass. However, the convective envelope mass alone cannot explain the full shape of the predicted (and observed) abundance pattern. It accounts

for the increasing depletion toward higher masses, but it does not explain why the depletion reaches a minimum and then becomes weaker again at higher masses. This turnover point is produced by the turbulent mixing ($D_T$) included in the MIST models (A. Dotter et al. 2017), following C. R. Proffitt & G. Michaud (1991) as modified by D. A. VandenBerg et al. (2012):

$$D_T = D_0 \left(\frac{\rho_{CZ}}{\rho}\right)^3 \left(\frac{M_{CZ}}{M_\star}\right)^{-3/2}, \quad (2)$$

with $D_0 = 1\,\mathrm{cm^2\,s^{-1}}$, calibrated on the metal-poor globular cluster NGC 6397. Evaluated at the base of the convection zone, where $\rho = \rho_{CZ}$, the turbulent-diffusion coefficient scales as $D_T \propto (M_{CZ}/M_\star)^{-3/2}$ and increases steeply as the convective envelope becomes thinner. In the models shown here, $D_T$ rises from $\sim$50 $\mathrm{cm^2\,s^{-1}}$ at $0.7\,M_\odot$ to $\gtrsim 10^7\,\mathrm{cm^2\,s^{-1}}$ at $1.4\,M_\odot$. At higher masses before the RGB, where the convective envelope becomes extremely shallow or effectively disappears ($M_\star \gtrsim 1.45\,M_\odot$), the computed values should be regarded as lower limits, shown as open triangles in Figure 2.

The predicted minimum [Fe/H] marks the transition between two competing regimes. On the low-mass side, surface depletion is limited by convective dilution: the deeper convective envelope mixes the settled material over a larger mass range. On the high-mass side, turbulent mixing becomes sufficiently efficient to counteract gravitational settling and restore the surface abundances toward their initial values. The mass at which these two effects balance ($M_\star \simeq 1.25\,M_\odot$), at near-solar composition, is set primarily by the stellar structure and by the adopted turbulent-mixing prescription and is only weakly sensitive to age over the range considered here for the two studied open clusters.

This nearly fixed abundance depletion as a function of mass, in contrast to the age-dependent turnoff mass, is central to the evolutionary interpretation of our sample. In NGC 752, at an age of 1.3 Gyr, the cluster turnoff occurs at $M_\star \gtrsim 1.78\,M_\odot$, whereas the stars showing the strongest depletion are concentrated around $M_\star \approx 1.2$–$1.35\,M_\odot$. In this regime, these are upper-main-sequence stars, and the abundance minimum in NGC 752 does not coincide with the cluster turnoff itself.

In Ruprecht 147, the older cluster age shifts the turnoff to lower masses, around $M_\star \simeq 1.5\,M_\odot$. This is much closer to the mass range where the MIST models predict the strongest surface-abundance depletion, near $M_\star \simeq 1.2$–$1.3\,M_\odot$, than in the younger NGC 752 cluster. Therefore, in Ruprecht 147 the stars classified as MS–TO are sampling the region immediately above the predicted abundance minimum, where the models begin to recover toward the initial cluster abundance. In other words, the diffusion-sensitive mass range and the observed turnoff region are closer to overlapping in Ruprecht 147, while they are clearly separated in NGC 752. It also explains why the depletion signature occurs at a lower effective temperature than in NGC 752 (see Figure 2, top panel).

Guided by this framework, we define five evolutionary classes, which are adopted consistently throughout the remainder of this paper:

1. *CS* (cool stars): the coolest unevolved members of the sample ($M_\star \lesssim 0.8\,M_\odot$ for NGC 752 and $M_\star \lesssim 1.0\,M_\odot$ for Ruprecht 147). These stars have deep convective envelopes ($\Delta m_{env}/M_\star \sim 10^{-1}$), which efficiently dilute the effects of gravitational settling. Their surface abundances are therefore expected to remain closest to the initial cluster composition.
2. *MS* (main sequence): unevolved main-sequence stars with $0.8 \lesssim M_\star/M_\odot \lesssim 1.2$. In this mass range, the convective envelope becomes progressively thinner as mass increases, but the predicted diffusion-driven depletion remains moderate.
3. *Diff* (diffusion-dominated): stars within the mass interval of maximum predicted surface depletion ($M_\star \approx 1.2$–$1.35\,M_\odot$; green band in Figure 2). These stars are the primary probes of atomic diffusion in this work.
4. *MS–TO* (main-sequence–turnoff): stars at, or just beyond, the MSTO of each cluster ($M_\star \gtrsim 1.78\,M_\odot$ in NGC 752 and $M_\star \simeq 1.5\,M_\odot$ in Ruprecht 147).
5. *RG* (red giants): evolved stars on the RGB. In these stars, the deepening convective envelope during the FDU has largely erased the surface-depletion signature of atomic diffusion, restoring the surface abundances toward values close to the initial cluster composition.

We expect both the CS and RG samples to provide the closest estimates of the initial cluster composition because their deep convective envelopes efficiently dilute or erase the surface-abundance signatures produced by atomic diffusion. However, RG stars are known to experience abundance changes during the FDU, particularly in C and N and, to a lesser extent, in Na. We therefore adopt the CS sample as our primary reference for the pristine open-cluster composition.

The bottom panels of Figure 2 show that, under this classification, the observed [Fe/H]–mass trends closely follow the model predictions in both clusters. Pink circles are the CS sample, green pentagons are the MS sample, yellow downward-pointing triangles are the Diff sample, orange plus signs are the MS–TO sample, and blue upward-pointing triangles are the RG sample. In NGC 752, the Diff-class stars reach [Fe/H] $\simeq -0.10$ to $-0.13$ dex, tracing the bottom of the predicted depletion trough. In contrast, the CS and MS stars scatter around the initial cluster composition, while the red giants recover near-initial abundances after FDU. In Ruprecht 147, a similar V-shaped profile is present, with the stars near the $1.2\,M_\odot$ occupying the depletion region. However, we see some stars near the turnoff remaining more depleted than the MIST isochrone predicts.

We note that the stellar masses are isochrone derived, and we adopt an uncertainty of $\pm 0.05\,M_\odot$, shown as horizontal error bars in the bottom panels of Figure 2. As an independent check, masses estimated using the empirical calibration of G. Torres et al. (2010) are consistent with the isochrone masses within these uncertainties. In the following subsection, we present the element-by-element abundance trends as a function of effective temperature, adopting the evolutionary classes defined above.

### 4.2. Abundance Trends as a Function of $T_{eff}$

In Figures 3 and 4, we show chemical abundances of the studied elements as a function of effective temperature for sample stars from the clusters NGC 752 and Ruprecht 147, respectively, with each panel representing a studied element. Markers are the same as in the bottom panel of Figure 2, where pink circles are the coolest stars (CS), green pentagons are the main sequence (MS), yellow downward-pointing triangles are most diffused stars (Diff), orange plus signs are the main-sequence–turnoff transition (MS–TO), and blue upward-

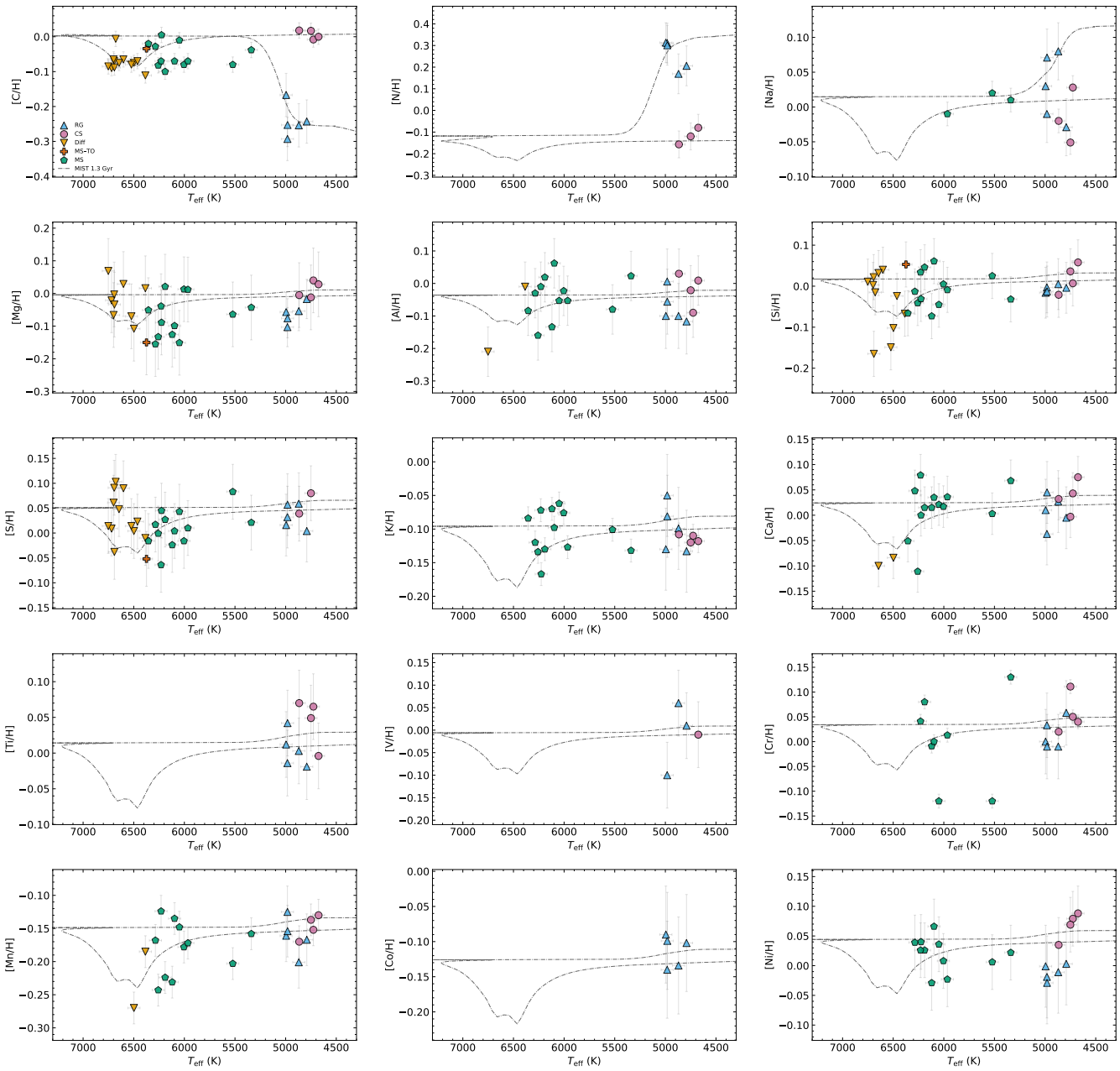


**Figure 3.** Abundances, [X/H], as a function of effective temperature of the studied elements for the open cluster NGC 752. Each panel corresponds to a different chemical species. The different symbols indicate the evolutionary stages: pink triangles represent red giant (RG) stars, green squares indicate main-sequence (MS) stars, yellow circles show stars in the main-sequence–turnoff transition region (MS–TO), and blue plus signs represent turnoff (TO) stars. The dotted–dashed curves show the MIST atomic diffusion model (J. Choi et al. 2016) for an age of 1.3 Gyr and [Fe/H] = 0.00.

pointing triangles are the red giant sample (RG). Gray error bars show the uncertainties in both $T_{\rm eff}$ and [Fe/H].

#### 4.2.1. Carbon

Carbon abundances in the APOGEE spectra are primarily derived from two sets of spectral features: atomic C I lines in the warmer MS and MS–TO stars, and molecular CO lines in the cooler CS and RG stars (V. V. Smith et al. 2013; D. Souto et al. 2018a). The carbon abundances in NGC 752 reveal a remarkably clean signature of stellar evolution: atomic diffusion in the Diff stars, and the onset of the FDU in the cooler red giants. Our derived abundances indicate a mean $\langle$[C/H]$\rangle$ of –0.07 ± 0.02 dex for the warmer Diff stars, –0.04 for the MS–TO, –0.05 ± 0.03 dex for the main-sequence end (MS), 0.01 ± 0.01 for the coolest stars (CS), and a significantly lower abundance for RG, with $\langle$[C/H]$\rangle$ = –0.24 ± 0.04 dex. The abundance difference between Diff and CS stars ($\Delta$(Diff − CS)) is −0.08. This difference is >3 times the typical abundance scatter in our measurements ($\sigma$), providing evidence for carbon depletion as a signature of atomic diffusion.

As shown in Figure 3, the determined carbon abundances in NGC 752 align closely with the model predictions, reinforcing the presence of both atomic diffusion in warmer stars and convective mixing in more evolved giants. At the cooler end, the behavior is consistent with the effects of the FDU, a well-understood mixing process that reduces surface carbon abundances by bringing CNO-processed material to the surface (N. Lagarde et al. 2012). Together, these abundance patterns provide compelling observational support for the

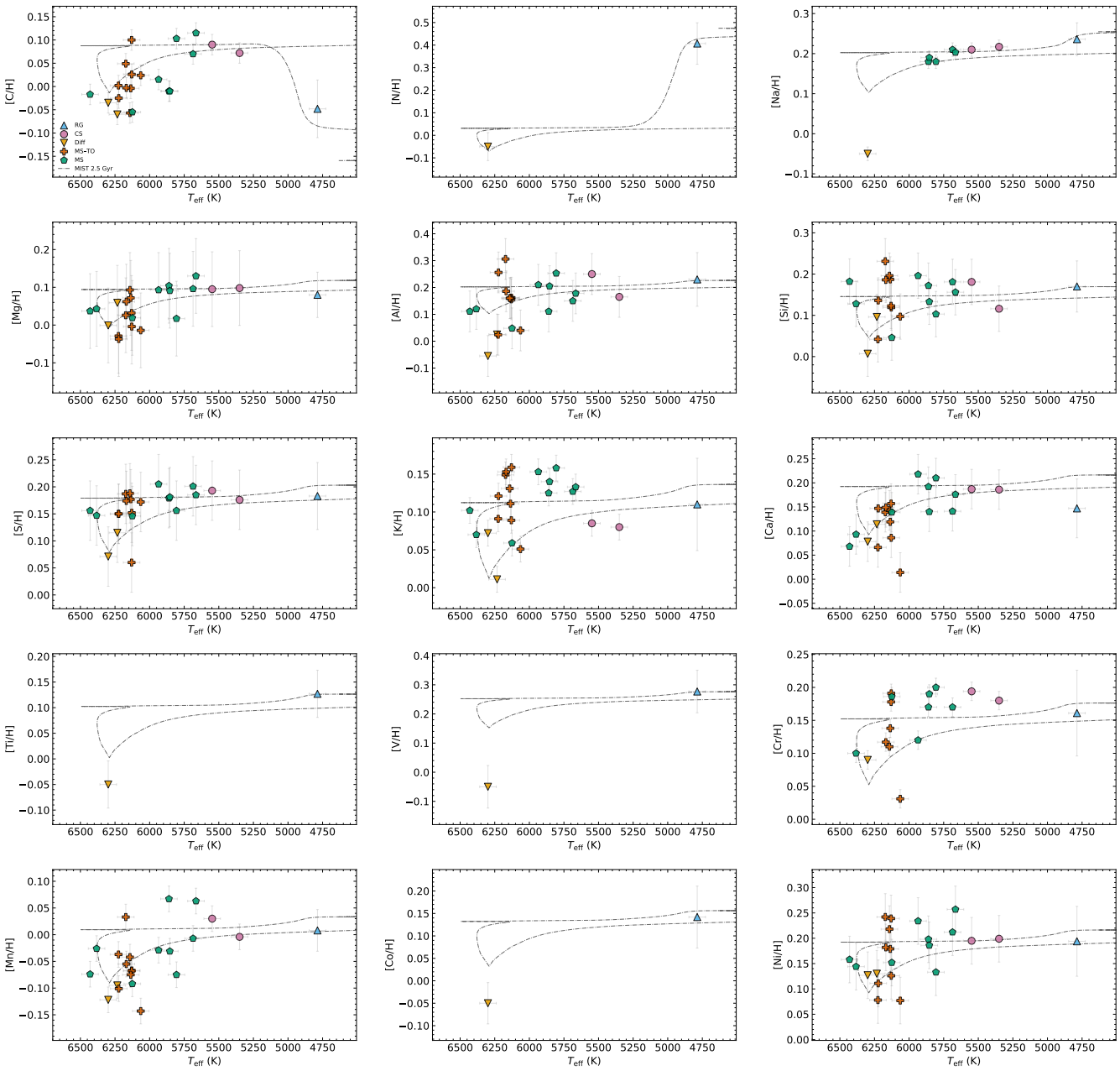


**Figure 4.** Abundances, [X/H], as a function of effective temperature of the studied elements for the open cluster Ruprecht 147. Each panel corresponds to a different chemical species. The different symbols indicate the evolutionary stages: pink triangles represent red giant (RG) stars, green squares indicate main-sequence (MS) stars, yellow circles show stars in the main-sequence–turnoff transition region (MS–TO), and blue plus signs represent turnoff (TO) stars. The dotted–dashed curves show the MIST atomic diffusion model (J. Choi et al. 2016) for an age of 2.5 Gyr and [Fe/H] = 0.18.

combined action of atomic diffusion and mixing in the chemical evolution of NGC 752 stars.

For Ruprecht 147, we also find evidence that atomic diffusion and mixing affect the surface abundances of Diff and red giant stars, respectively. The CS stars yield $\langle$[C/H]$\rangle = 0.08 \pm 0.01$ dex, which we adopt as representative of the cluster's pristine carbon abundance. In comparison, the Diff stars show lower carbon abundances, with $\langle$[C/H]$\rangle$ = –0.04 ± 0.02 dex, whereas the MS–TO has $\langle$[C/H]$\rangle = 0.01 \pm 0.05$ dex. The RG star has a carbon abundance of $\langle$[C/H]$\rangle = -0.05 \pm 0.00$ dex,[8] in the same scale as consistent with carbon depletion caused by the FDU. The derived $\Delta$(Diff − CS) is −0.13 with $>3\sigma$ confidence level. It indicates that atomic diffusion operates in the carbon abundances of Ruprecht 147.

Figure 4 follows the same format as Figure 3, but for the Ruprecht 147 open cluster. The carbon abundances of the Diff population and the MS–TO population lie near the depletion level predicted by the MIST isochrones, consistent with the expected signature of atomic diffusion. The lower carbon abundance measured for the RG star is also consistent with carbon depletion associated with FDU.

#### 4.2.2. Nitrogen

Nitrogen abundances in APOGEE spectra are derived from several well-defined CN molecular lines. Because these

[8] We report a standard deviation of zero to indicate that either only one star has a precise carbon abundance measurement or all the derived abundances converged to the same value.

molecular features are highly sensitive to $T_{\rm eff}$, we cannot reliably determine nitrogen abundances for the warmer MS–TO and Diff stars. Therefore, we cannot directly probe the signature of atomic diffusion in nitrogen for either cluster.

Figure 3 shows a clear signature of extra mixing in NGC 752, as indicated by the enhanced nitrogen abundance of the red giant stars. We obtain $\langle$[N/H]$\rangle = -0.12 \pm 0.04$ dex for the CS stars and $\langle$[N/H]$\rangle = 0.26 \pm 0.07$ dex for the RG stars. A similar behavior is seen in Figure 4 for Ruprecht 147. However, in this cluster we lack nitrogen abundances for the MS stars and have only one RG star with a nitrogen measurement, yielding [N/H] = 0.35 ± 0.04 dex.

#### 4.2.3. Sodium

Sodium abundances are derived from two weak neutral Na I lines in the APOGEE spectra ($\lambda\lambda$16373.850 and 16388.860). In warmer stars, both features become increasingly weak, making precise sodium abundance determinations challenging. As a result, we could not derive reliable Na abundances for the Diff stars in NGC 752 and therefore cannot directly probe atomic diffusion of sodium in that cluster.

The previous work by V. Loaiza-Tacuri et al. (2023) has shown that the Na abundances of red giants belonging to the young open cluster NGC 6705 (age = 316; turnoff mass = 3.3 $M_{\odot}$) show sodium enhancements ([Na/Fe] = +0.29), in agreement with expectations from FDU on the RGB of models by N. Lagarde et al. (2012). The open clusters in this study, NGC 752 and Ruprecht 147, have significantly older ages and lower turnoff masses and are expected to show much less Na enhancement, due to mixing. For NGC 752, we obtain $\langle$[Na/H]$\rangle$ = −0.00 ± 0.04 dex, 0.01 ± 0.02 dex, and 0.03 ± 0.05 dex for the CS, MS, and RG stars, respectively. For Ruprecht 147, we determine $\langle$[Na/H]$\rangle$ = 0.21 ± 0.01 dex, 0.19 ± 0.00 dex, and 0.24 ± 0.00 dex for the same evolutionary groups. In both clusters, the CS and MS abundances agree within the uncertainties, while the RG stars show slightly higher Na abundances. This behavior is visible in Figures 3 and 4, where the Na enhancement in the red giants is generally consistent with the MIST predictions and with the effects of extra mixing operating in the convective envelopes of red giant stars (e.g., N. Lagarde et al. 2012). We find a clear signature of atomic diffusion in Ruprecht 147, with Δ(Diff − CS) of −0.26. This is the largest difference in abundance among the stellar classes analyzed in this work.

#### 4.2.4. Magnesium

The APOGEE spectra contain six well-defined Mg I lines that can be used to derive magnesium abundances. However, three of the strongest features, at 15740.72, 15748.99, and 15765.84 Å, which are shown in the right panel of Figure 1, are known to exhibit strong systematic abundance trends with effective temperature in the dwarf stars, being particularly biased for the K dwarfs (V. Grilo et al. 2024). We excluded these three Mg I lines from the present analysis. Instead, we used the Mg I lines at 15879.50, 15886.20, and 15954.48 Å, which provide more reliable diagnostics for investigating abundance trends associated with stellar evolution.

For the NGC 752 open cluster, our analysis yields $\langle$[Mg/H]$\rangle$ = 0.01 ± 0.03 dex, −0.01 ± 0.06 dex, −0.02 ± 0.05 dex, −0.015 ± 0.00 dex, and −0.06 ± 0.03 dex for the CS, MS, Diff, MS–TO, and RG stars, respectively. The abundance difference between the Diff and CS stars is Δ(Diff − CS) = −0.03 dex, significant at the 1.5$\sigma$ level. As shown in Figure 3, [Mg/H] follows a temperature-dependent trend broadly consistent with the predictions of diffusion models, supporting the operation of atomic diffusion in NGC 752.

A similar behavior is found for Ruprecht 147. We obtain $\langle$[Mg/H]$\rangle$ = 0.10 ± 0.00 dex, 0.07 ± 0.04 dex, 0.03 ± 0.04 dex, 0.02 ± 0.05 dex, and 0.08 ± 0.00 dex for the CS, MS, Diff, MS–TO, and RG stars, respectively. In this case, Δ(Diff − CS) = −0.07 dex, significant at the 2.2$\sigma$ level, providing additional evidence for atomic diffusion in Ruprecht 147. Figure 4 shows this behavior, with most Diff and MS–TO stars overall following the expected abundance dip associated with diffusion.

We note, however, that the RG [Mg/H] values fall slightly below the MIST evolutionary tracks in both clusters, as seen in Figures 3 and 4. Magnesium also exhibits some of the largest abundance uncertainties in our sample, ranging from ∼0.06 dex for RG stars to ∼0.10 dex for TO and MS stars. These larger uncertainties likely contribute to the increased dispersion in abundance observed in the figures but cannot explain systematic differences.

#### 4.2.5. Aluminum

Aluminum abundances are derived from three well-defined Al I lines in the redder region of the APOGEE spectra. However, as with the Mg I features discussed above, two of these Al I lines, at 16719 and 16750.6 Å, show systematic abundance trends with effective temperature in dwarfs and are therefore excluded from our analysis. We use only one Al I line at 16763.4 Å. Although this leaves a single diagnostic feature, it provides the most reliable aluminum indicator for investigating abundance trends associated with stellar evolution and for searching for signatures of atomic diffusion.

For NGC 752, the diagnostic Al I line is not sufficiently well defined in the MS–TO stars to allow precise abundance determinations. For the CS, MS, Diff, and RG stars, we obtain $\langle$[Al/H]$\rangle = -0.02 \pm 0.05$ dex, $-0.04 \pm 0.07$ dex, $-0.11 \pm 0.14$ dex, and $-0.07 \pm 0.05$ dex, respectively. Similar to Mg, the Al abundances show a relatively large scatter, likely driven by their larger typical uncertainties (∼0.06–0.10 dex), as seen in Figure 3. The Δ(Diff − CS) is −0.09 dex, significant at the ∼1$\sigma$ level. Figure 3 shows the overall behavior of the Diff stars following the expected diffusion-induced abundance dip.

We find a clear signature of atomic diffusion in Ruprecht 147, with Δ(Diff − CS) = −0.22 dex, significant at the >3$\sigma$ level. We derive $\langle$[Al/H]$\rangle$ = 0.21 ± 0.06 dex, 0.16 ± 0.06 dex, −0.2 ± 0.06 dex, 0.16 ± 0.09 dex, and 0.23 ± 0.00 dex for the CS, MS, Diff, MS–TO, and RG stars, respectively. Figure 4 shows [Al/H] as a function of the effective temperature, where the Al abundances also exhibit larger scatter than most other elements.

#### 4.2.6. Silicon

Nine Si I lines are available for deriving silicon abundances from APOGEE spectra. As discussed by V. Grilo et al. (2024), four of these lines, at 15888.4, 15960.1, 16060.0, and 16094.8 Å, show strong systematic trends with $T_{\rm eff}$ for the dwarfs. We therefore exclude these features from the present analysis and use only five Si I lines at 15361.2, 15376.8, 16215.7, 16680.8, and 16828.2 Å.

We find strong evidence for atomic diffusion affecting silicon abundances in the Diff stars of NGC 752, with $\Delta(\mathrm{Diff}-\mathrm{CS}) = -0.06$ dex at a significance level of $2.1\sigma$. The CS, MS, MS–TO, and RG stars have similar abundances, with $\langle[\mathrm{Si/H}]\rangle = 0.02 \pm 0.03$ dex, $-0.01 \pm 0.04$ dex, $0.05 \pm 0.00$ dex, and $-0.01 \pm 0.01$ dex, respectively. In contrast, the Diff stars show a systematically lower abundance, $[\mathrm{Si/H}] = -0.04 \pm 0.07$ dex, as expected from atomic diffusion. This behavior is shown in Figure 3. We also note that the Si abundances display a smaller typical scatter than the Mg and Al abundances discussed above.

A similar result is obtained for Ruprecht 147. For this cluster, we derive $\langle[\mathrm{Si/H}]\rangle = 0.15 \pm 0.05$ dex, $0.15 \pm 0.05$ dex, $0.05 \pm 0.06$ dex, $0.15 \pm 0.06$ dex, and $0.17 \pm 0.00$ dex for the CS, MS, Diff, MS–TO, and RG stars, respectively. We obtain $\Delta(\mathrm{Diff}-\mathrm{CS}) = -0.10$ dex at a significance level of $1.8\sigma$, suggesting that atomic diffusion also affects the silicon abundances in Ruprecht 147.

#### 4.2.7. Sulfur

For sulfur, we identify eight well-defined S I lines in the APOGEE spectra, at 15400.1, 15402.3, 15403.8, 15406.0, 15422.3, 15469.8, 15475.6, and 15478.5 Å. These features are stronger in warmer stars and become progressively weaker toward lower effective temperatures.

For NGC 752, we obtain $\langle[\mathrm{S/H}]\rangle = 0.06 \pm 0.03$ dex, $0.01 \pm 0.04$ dex, $0.03 \pm 0.04$ dex, $-0.05 \pm 0.00$ dex, and $0.03 \pm 0.02$ dex for the CS, MS, Diff, MS–TO, and RG stars, respectively. The abundance difference between the Diff and CS stars is $\Delta(\mathrm{Diff}-\mathrm{CS}) = -0.03$ dex, significant at the $1.1\sigma$ level. As shown in Figure 3, the overall sulfur abundance pattern follows the MIST isochrone for the cluster, with the lowest abundances occurring near the turnoff.

For Ruprecht 147, we obtain $\langle[\mathrm{S/H}]\rangle = 0.18 \pm 0.01$ dex, $0.17 \pm 0.02$ dex, $0.09 \pm 0.03$ dex, $0.16 \pm 0.04$ dex, and $0.18 \pm 0.00$ dex for the CS, MS, Diff, MS–TO, and RG stars, respectively. The abundance difference between the Diff and CS stars is $\Delta(\mathrm{Diff}-\mathrm{CS}) = -0.09$ dex, significant at the $>3\sigma$ level. As shown in Figure 4, for the two studied open clusters, the sulfur abundances display a smooth expected depletion toward the TO region, broadly consistent with the behavior predicted by the MIST diffusion models.

#### 4.2.8. Potassium

Potassium abundances are derived from two K I lines located near the beginning of the blue APOGEE detector, at 15163.1 and 15168.4 Å. This spectral region can be affected by persistence effects, as discussed by J. A. Holtzman et al. (2018). However, we find no evidence that persistence significantly affected the spectra analyzed in this work.

For NGC 752, we derive $\langle[\mathrm{K/H}]\rangle = -0.11 \pm 0.01$ dex, $-0.11 \pm 0.03$ dex, and $-0.10 \pm 0.04$ dex for the CS, MS, and RG stars, respectively. We are unable to derive reliable potassium abundances for the Diff and MS–TO stars because the K I lines are too weak in the warmer stellar spectra; therefore, it is expected that our sample cannot properly probe the effects of diffusion for this element. Within the uncertainties, the potassium abundances remain nearly constant across the different evolutionary stages, showing no statistically significant abundance trend associated with atomic diffusion or extra mixing. As shown in Figure 3, the [K/H] abundances exhibit relatively small scatter and remain broadly consistent with a constant abundance pattern across the cluster sequence.

For Ruprecht 147, on the other hand, the MIST model shown in Figure 4 indicates that the diffusion dip occurs at a cooler effective temperature of around 6250 K. We derive $\langle[\mathrm{K/H}]\rangle = 0.08 \pm 0.01$ dex, $0.12 \pm 0.04$ dex, $0.04 \pm 0.04$ dex, $0.12 \pm 0.04$ dex, and $0.11 \pm 0.00$ dex for the CS, MS, Diff, MS–TO, and RG stars, respectively. The Diff stars exhibit systematically lower potassium abundances relative to the other evolutionary stages, with $\Delta(\mathrm{Diff}-\mathrm{CS}) = -0.04$ dex at a significance level of $1.3\sigma$. This is evidence of atomic diffusion operating in the potassium abundances of Ruprecht 147 stars. As shown in Figure 4, the overall abundance pattern follows the expected depletion near the turnoff predicted by the MIST diffusion models, while the RG abundance returns to values comparable to those observed in the CS and MS stars.

#### 4.2.9. Calcium

There are four well-defined Ca I lines in the APOGEE spectra, at 16136.8, 16150.8, 16155.236, and 16157.4 Å, which can be used to derive precise calcium abundances. These features are located in a relatively narrow spectral region. However, the Ca I line at 16155.236 Å is often blended with other species and is excluded from our analysis.

For NGC 752, calcium shows one of the clearest abundance separations for the Diff stars. We obtain $\langle[\mathrm{Ca/H}]\rangle = 0.04 \pm 0.03$ dex, $0.01 \pm 0.05$ dex, $-0.09 \pm 0.01$ dex, and $0.01 \pm 0.03$ dex for the CS, MS, Diff, and RG stars, respectively. The Diff abundance is substantially lower than the CS abundance, yielding $\Delta(\mathrm{Diff}-\mathrm{CS}) = -0.13$ dex with a significance of $>3\sigma$. This strong offset indicates a pronounced calcium depletion at 1.2 $M_{\odot}$, consistent with the expected effect of atomic diffusion. In contrast, the RG abundance is comparable to the CS value, suggesting that the surface calcium depletion is largely erased after the deepening of the convective envelope during post-main-sequence evolution. Figure 3 shows this behavior, and we can see a group of Diff stars falling at the bottom of the MIST isochrone, where we expect the stronger signature of atomic diffusion.

For the open cluster Ruprecht 147, the calcium abundances show a similar evolutionary pattern. We derive $\langle[\mathrm{Ca/H}]\rangle = 0.18 \pm 0.01$ dex, $0.15 \pm 0.05$ dex, $0.10 \pm 0.03$ dex, $0.11 \pm 0.05$ dex, and $0.15 \pm 0.00$ dex for the CSS, MS, Diff, MS–TO, and RG stars, respectively. The Diff stars are systematically more Ca-poor than the CS stars, giving $\Delta(\mathrm{Diff}-\mathrm{CS}) = -0.09$ dex at a significance level of $>3\sigma$. Although less significant than in NGC 752, this offset still supports the presence of atomic diffusion in Ruprecht 147, from the smooth agreement between the derived abundance pattern and the MIST isochrone, as shown in Figure 4.

#### 4.2.10. Chromium

Chromium abundances are derived from a single weak Cr I line in the APOGEE spectra, at 15680.1 Å. For NGC 752, we obtain $\langle[\mathrm{Cr/H}]\rangle = 0.06 \pm 0.04$ dex, $0.02 \pm 0.09$ dex, and $0.01 \pm 0.03$ dex for the CS, MS, and RG stars, respectively. The CS and MS abundances agree within the uncertainties, and the RG abundance is also consistent with the same abundance scale. We note that the typical scatter in Cr is generally larger than for several other species, likely because the abundance determination relies on a single weak Cr I feature. Since

reliable Cr abundances are unavailable for the Diff stars, where this line is too weak, we cannot directly evaluate the expected turnoff depletion of this element in NGC 752. Figure 3 shows that the Cr abundances are more scattered within the evolutionary stages, particularly among the MS stars.

For Ruprecht 147, as previously, the model diffusion dip is cooler, and chromium provides a strong indication of abundance depletion at the Diff stars. We derive $\langle$[Cr/H]$\rangle$ = 0.19 ± 0.01 dex, 0.16 ± 0.04 dex, 0.09 ± 0.00 dex, 0.13 ± 0.06 dex, and 0.16 ± 0.00 dex for the CS, MS, Diff, MS–TO, and RG stars, respectively. The Diff abundance is substantially lower than the CS value, yielding $\Delta$(Diff − CS) = −0.10 dex with a significance of $>3\sigma$. This large offset suggests pronounced chromium depletion in the Diff stars, consistent with the expected signature of atomic diffusion. The MS–TO stars remain closer to the MS abundance scale, as shown in Figure 4.

#### 4.2.11. Manganese

The APOGEE spectral coverage includes three Mn I lines in the blue region of the detector, at 15159.0, 15217.8, and 15262.4 Å. As discussed for the potassium abundances, this spectral region can be affected by persistence. However, we do not find evidence that persistence significantly impacted the spectra analyzed in this work.

For NGC 752, manganese shows a clear decrease in abundance toward the TO region. We obtain $\langle$[Mn/H]$\rangle$ = −0.15 ± 0.02 dex, −0.18 ± 0.04 dex, −0.23 ± 0.06 dex, and −0.16 ± 0.03 dex for the CS, MS, Diff, and RG stars, respectively. No MS–TO abundance could be derived for Mn. The Diff abundance is significantly lower than the CS abundance, yielding $\Delta$(Diff − CS) = −0.08 dex at the $1.8\sigma$ level. This offset suggests substantial manganese depletion in the Diff star, consistent with the expected signature of atomic diffusion. Figure 3 summarizes this behavior.

For Ruprecht 147, the manganese abundances also show a clear depletion at the Diff point. We obtain $\langle$[Mn/H]$\rangle$ = 0.01 ± 0.02 dex (CS), 0.02 ± 0.06 dex (MS), −0.11 ± 0.02 dex (Diff), −0.06 ± 0.05 dex (MS–TO), and 0.01 ± 0.00 dex (RG). The abundance difference between the Diff and CS stars is $\Delta$(Diff − CS) = −0.12 dex, significant at the $>3\sigma$ level. This offset indicates a strong manganese depletion in the Diff stars, consistent with the expected signature of atomic diffusion. The MS–TO stars show intermediate abundances, while the RG abundance is comparable to the MS value, suggesting that the diffusion signature is largely reduced after post-main-sequence evolution, as shown in Figure 4.

#### 4.2.12. Titanium, Vanadium, and Cobalt

Titanium, vanadium, and cobalt are grouped together in this analysis because we are unable to determine reliable abundances for the warmer stars in NGC 752 and for the CS sample in Ruprecht 147, where we derive abundances for one Diff star and one RG star. For Ti, six well-defined Ti I lines are available in the APOGEE spectra. Following the recommendation of V. Grilo et al. (2024), we use only the three lines that do not show systematic abundance trends with effective temperature, at 15602.8, 15699.0, and 16635.2 Å. The remaining Ti I lines, at 15334.8, 15543.8, and 15715.6 Å, are excluded from this work. For V and Co, only one weak line is available in the APOGEE spectral coverage, at 15924.9 and 16757.7 Å, respectively.

In NGC 752, we derive titanium abundances of $\langle$[Ti/H]$\rangle$ = 0.05 ± 0.03 dex and 0.01 ± 0.02 dex for the CS and RG stars, respectively. Titanium is a challenging element to study in APOGEE spectra because its abundances often show larger scatter and/or systematic offsets when compared with benchmark stars (see discussion in D. Souto et al. 2016, 2019; H. Jönsson et al. 2020). In this work, however, we find a relatively small scatter for both the CS and RG samples, with standard deviations of 0.03 and 0.02 dex, respectively. This improvement may be related to our more restrictive line selection, in which we exclude Ti I features known to display systematic abundance trends. For vanadium, both the CS and RG stars yield $\langle$[V/H]$\rangle$ = −0.01 dex, with standard deviations of 0.00 and 0.08 dex, respectively. Cobalt abundances could only be derived for the red giant stars, for which we obtain $\langle$[Co/H]$\rangle$ = −0.11 ± 0.02 dex.

In Ruprecht 147, abundances for these elements could only be determined for the Diff and red giant stars, for which we obtain $\langle$[Ti/H]$\rangle$ = −0.05 and 0.13 dex, [V/H] = −0.05 and 0.28 dex, and $\langle$[Co/H]$\rangle$ = −0.05 and 0.14 dex, respectively. These measurements are shown in Figure 4, and if we consider the RG star to indicate the pristine cluster composition, we can indicate that atomic diffusion is operating in these elements.

#### 4.2.13. Nickel

We used seven well-defined Ni I lines (at 15605.7, 15632.7, 16584.4, 16589.3, 16673.7, 16815.5, and 16818.8 Å) to derive nickel abundances from the APOGEE spectra of the sample stars.

For NGC 752, we were unable to derive Ni abundances for Diff stars to probe the signature of atomic diffusion. For the other stellar classes, we obtained $\langle$[Ni/H]$\rangle$ = 0.07 ± 0.02 dex (CS), 0.02 ± 0.03 dex (MS), and –0.01 ± 0.01 dex (RG). The CS and MS abundances are consistent within the uncertainties, and the RG abundance is only slightly lower. As shown in Figure 3, the Ni abundance distribution remains relatively flat across the available evolutionary stages, as we also lack MS–TO stars with higher $T_{\rm eff}$, suggesting that nickel does not provide a strong diagnostic of atomic diffusion in NGC 752 with the present sample.

For Ruprecht 147, on the other hand, the nickel abundances show a clear depletion in the Diff sample. We obtain $\langle$[Ni/H]$\rangle$ = 0.20 ± 0.01 dex (CS), 0.19 ± 0.04 dex (MS), 0.13 ± 0.00 dex (Diff), 0.16 ± 0.06 dex (MS–TO), and 0.19 ± 0.00 dex (RG). The Diff stars are systematically more Ni-poor than the CS stars, yielding $\Delta$(Diff − CS) = −0.07 dex at $>3\sigma$ significance. This offset suggests that nickel is also affected by atomic diffusion in Ruprecht 147. The MS and MS–TO stars show intermediate abundances, while the RG abundance is closer to the CS abundance scale, as shown in Figure 4.

#### 4.2.14. Iron

Several Fe I lines are present in the APOGEE spectra. In this work, we analyzed 77 Fe I features but excluded 25 lines from the final abundance determination, following the recommendation of V. Grilo et al. (2024), to avoid transitions that exhibit systematic abundance trends with $T_{\rm eff}$. We note that for cooler stars such as late K and M dwarfs roughly 30 well-defined FeH lines can also serve as iron abundance

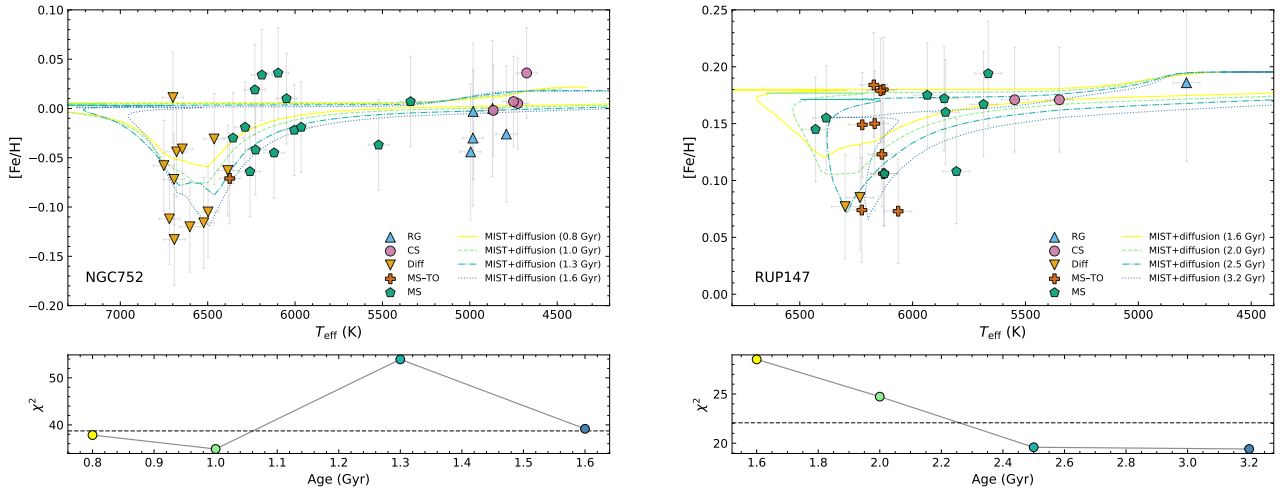


**Figure 5.** Top left: metallicity as a function of effective temperature for NGC 752. The solid and dashed lines represent MIST isochrones assuming [Fe/H] = –0.05 and ages = 0.8, 1.0, 1.3, 1.6 Gyr. Bottom left: a chi-squared minimization comparing the derived metallicities with MIST isochrones. The gray dashed line is a chi-squared comparison assuming that the mean metallicity is constant. The colors of the circles correspond to the five models shown above, which are used to calculate their chi-squared value. The right panels are similar to the left panels, but for Ruprecht 147, where the MIST isochrones assume [Fe/H] = 0.12 and ages = 1.6, 2.0, 2.5, 3.2 Gyr.

diagnostics (D. Souto et al. 2017, 2018b, 2026). However, these FeH transitions are not detected in the K dwarfs analyzed in this work.

For NGC 752, iron shows a clear depletion pattern in the Diff sample. We obtain $\langle$[Fe/H]$\rangle$ = 0.01 ± 0.02 dex, −0.01 ± 0.03 dex, −0.07 ± 0.04 dex, −0.07 ± 0.00 dex, and −0.02 ± 0.02 dex for the CS, MS, Diff, MS–TO, and RG stars, respectively. The Diff stars are systematically more Fe-poor than the CS stars, yielding $\Delta$(Diff − CS) = −0.09 dex at a significance level of $>3\sigma$. This strong offset provides one of the clearest signatures of atomic diffusion in NGC 752, as shown in Figure 3, where the Diff sample falls right at the expected atomic diffusion model.

A similar conclusion is obtained for Ruprecht 147, as iron also shows a clear abundance depletion in the Diff sample. We obtain $\langle$[Fe/H]$\rangle$ = 0.17 ± 0.00 dex (CS), 0.15 ± 0.03 dex (MS), 0.08 ± 0.01 dex (Diff), 0.13 ± 0.04 dex (MS–TO), and 0.19 ± 0.00 dex (RG). We obtain a $\Delta$(Diff − CS) = −0.09 dex at a significance level of $>3\sigma$. This strong offset provides robust evidence that atomic diffusion affects the surface iron abundances in Ruprecht 147. Figure 4 shows a clear trend where these Diff stars are right at the dip of atomic diffusion in Ruprecht 147.

We also performed a quantitative comparison between the observed [Fe/H] abundances derived in this study and the MIST isochrone predictions for different ages, using a chi-squared minimization approach. The results for NGC 752 and Ruprecht 147 are presented in Figure 5, in the left and right panels, respectively. The atomic diffusion models used for the comparison with the NGC 752 stars (top left panel of Figure 5) correspond to ages of 800 Myr, 1.0 Gyr, 1.3 Gyr, and 1.6 Gyr. For Ruprecht 147, the models (top right panel of Figure 5) cover ages of 1.6, 2.0, 2.5, and 3.2 Gyr. The model points used in our $\chi^2$ comparison were carefully selected to match the observed stellar parameters ($T_{\rm eff}$, log $g$, and [Fe/H]) as closely as possible. This ensures that stars are compared at the correct stage of their evolution. Failure to constrain all three parameters can lead to incorrect matches between observed stars and model points, particularly since stars in different evolutionary phases (e.g., main sequence and RGB) may share similar effective temperatures and metallicities, as illustrated in Figures 3 and 4.

The dashed gray horizontal lines in the bottom panels of Figure 5 represent the $\chi^2$ values obtained by assuming a constant mean [Fe/H] for all evolutionary phases: –0.03 dex for NGC 752 (left) and +0.14 dex for Ruprecht 147 (right). This baseline model assumes no variation in surface [Fe/H] with evolutionary phase, serving as a reference to assess whether atomic diffusion improves the agreement between observations and theory. To perform this comparison consistently, all metallicities were converted from logarithmic to linear space before computing the $\chi^2$ values.

For NGC 752, the MIST models including atomic diffusion provide a better description of the observed [Fe/H] pattern than a constant-abundance model. In particular, the diffusion models reproduce the abundance depression observed near $T_{\rm eff}$ = 6500 K and the partial recovery toward cooler and more evolved stars. This is reflected in the lower $\chi^2$ values relative to the constant [Fe/H] model, with the best agreement obtained for the 1.0 Gyr isochrone. The improvement in $\chi^2$ indicates that the observed abundance variations are not simply random scatter around a single cluster metallicity but instead trace a temperature-dependent pattern consistent with atomic diffusion.

A similar result is obtained for Ruprecht 147. In this case, the diffusion models also yield lower $\chi^2$ values than the constant-abundance model, with the best fit obtained for the 2.5–3.2 Gyr isochrone. The agreement between the observed depletion and the predicted diffusion pattern provides an independent way to probe the cluster's evolutionary state, and potentially its age, using chemical abundances alone. For comparison, photometric isochrone fitting based on Gaia data yields ages of 1.3 Gyr for NGC 752 and 2.5 Gyr for Ruprecht 147 (T. Cantat-Gaudin et al. 2020), in good agreement with the ages favored by our abundance-based $\chi^2$ comparison.

These results suggest that atomic diffusion signatures in open clusters not only are useful for testing the physical processes operating during stellar evolution but also may provide an additional chemical clock for constraining cluster

ages. This is particularly valuable because the method is based on the relative abundance pattern along the cluster sequence, rather than on photometry alone. However, we emphasize that this approach depends on the precision of the abundance measurements, the adopted stellar models, and the treatment of additional mixing processes that can moderate the effects of atomic diffusion.

### 4.3. Consequences of Diffusion

Combining the results of this study for the open clusters NGC 752 and Ruprecht 147 with those, also from analyses of APOGEE spectra, from D. Souto et al. (2018a) for the older M67 open cluster (age $\sim$ 4.0 Gyr; A. Sarajedini et al. 2009) and from D. Souto et al. (2021) for the younger Coma Berenices open cluster (age $\sim$ 600 Myr, M. A. Agüeros et al. 2025), we find that atomic diffusion can have a significant impact on the measured surface abundances of stars near the MSTO and along the SGB. The results from this work reinforce previous findings and the importance of considering atomic diffusion.

In particular, care should be taken when interpreting observed metallicities of stars around the turnoff without accounting for atomic diffusion. This omission may result in the selection of isochrones that are too metal-poor compared to the star's birth composition, leading to a systematic overestimation of stellar ages. The earlier conclusions of D. A. VandenBerg et al. (2002) indicated that neglecting atomic diffusion can bias age estimates by up to 10%. As more clusters exhibit evidence of atomic diffusion signatures, these effects must be taken into account in both stellar modeling and age determinations, particularly for field stars. A. Dotter et al. (2017) further showed that assuming a constant metallicity in isochrone fitting, rather than allowing for metallicity variations due to diffusion, can lead to age overestimates of up to 20%. Failing to account for this process introduces a systematic offset in derived ages, which can propagate into errors in Galactic archeology studies and reconstructions of the Milky Way's formation history.

While this study does not yet provide a complete framework for correcting surface abundances back to their primordial values, it highlights the need for future work aimed at quantifying the impact of diffusion across a broad range of cluster ages and metallicities. Achieving this goal will require high-SNR, high-precision abundance measurements in open clusters with well-sampled evolutionary sequences, including stars on the main sequence, TO, SGB, and RGB. Such studies will be essential for mapping diffusion-induced abundance changes and recovering more accurate stellar ages in both cluster and field star populations.

## 5. Conclusions

In this work, we determine stellar parameters ($T_{\rm eff}$, $\log g$, $\xi$) and elemental abundances for Fe, C, N, Na, Mg, Al, Si, S, K, Ca, Ti, V, Cr, Mn, Co, and Ni for stars at different evolutionary stages in two open clusters: NGC 752 and Ruprecht 147. This work sample is designed to investigate whether there are signatures of atomic diffusion in these open clusters. For each cluster, we divide the sample into five evolutionary groups: the coolest stars in the sample (CS), the main sequence (MS), the stars most likely to present an atomic diffusion signature based on their mass (Diff), the main-sequence–turnoff transition (MS–TO), and red giant stars (RG).

Atomic diffusion has often been treated as a second-order effect in stellar abundance studies, but our results show that it produces measurable signatures in both NGC 752 and Ruprecht 147. For every element with reliable Diff abundances, the Diff stars are systematically depleted relative to the CS reference population, with offsets significantly above the $2\sigma$ level in both clusters. For example, averaging over all elements with abundances measured in both stellar classes off Diff and CS, we find $\langle\Delta(\mathrm{Diff}-\mathrm{CS})[\mathrm{X/H}]\rangle = -0.08 \pm 0.01$ dex for NGC 752 and $-0.12 \pm 0.01$ dex for Ruprecht 147. In both clusters, these offsets are significant at more than the $3\sigma$ level, confirming that stars in the diffusion-dominated regime are systematically depleted relative to the cool-star reference population. We also find evidence for post-main-sequence mixing in the carbon and sodium abundances of red giant stars. Carbon is especially diagnostic, as it traces both the depletion caused by atomic diffusion and the abundance changes produced by FDU and extra mixing in evolved stars. These results demonstrate that stellar evolution effects must be accounted for when interpreting precise chemical abundances in open clusters.

Using the atomic diffusion signature in the Fe abundances, we modeled the $T_{\rm eff}$–[Fe/H] distribution with MIST isochrones, including diffusion over a range of cluster ages. A $\chi^2$ comparison between the observed abundances and the model predictions gives the best agreement for the 1.0 Gyr isochrone in NGC 752 and the 2.5–3.2 Gyr isochrone in Ruprecht 147. These age estimates are based solely on the stellar chemical abundance patterns and are in excellent agreement with the cluster ages derived from Gaia photometry by T. Cantat-Gaudin et al. (2020). This result suggests that atomic diffusion signatures in open clusters not only are valuable probes of the physical processes operating during stellar evolution but also may provide an independent chemical clock for constraining cluster ages.

With the advent of ESA's Gaia mission, we are now able to determine precise absolute magnitudes for stars near the MSTO—precisely where the effects of atomic diffusion are expected to be strongest. Ignoring atomic diffusion in this regime leads to systematically underestimated metallicities and, consequently, biased age determinations. As large-scale spectroscopic surveys increasingly target these evolutionary phases (e.g., GALAH; M. R. Hayden et al. 2022), neglecting the effects of atomic diffusion will introduce systematics that may compromise our understanding of Galactic evolution. A broader sample of open clusters with full evolutionary coverage (including the main sequence, turnoff, SGB, and RGB) is essential to calibrate the surface-abundance variations induced by atomic diffusion. We aim to address this need in future work by expanding the number and diversity of open clusters analyzed.

## Acknowledgments

We thank the referee for giving good suggestions that helped improve the paper. D.S. acknowledges support from the Foundation for Research and Technological Innovation Support of the State of Sergipe (FAPITEC/SE) and the National Council for Scientific and Technological Development (CNPq), under grant Nos. 404056/2021-0, 794017/2013, and 444372/2024-5. T.S., P.M.F., K.C., A.I.W., and

N.M. acknowledge support for this research from the National Science Foundation Astronomy and Astrophysics grants AST-1715662, AST-2206541, and AST-2206543. P.M.F. and J.T. acknowledge that this work was performed at the Aspen Center for Physics, which is supported by National Science Foundation grant PHY-1607611.

Funding for the Sloan Digital Sky Survey IV has been provided by the Alfred P. Sloan Foundation, the US Department of Energy Office of Science, and the Participating Institutions.

SDSS-IV acknowledges support and resources from the Center for High Performance Computing at the University of Utah. The SDSS website is www.sdss.org.

SDSS-IV is managed by the Astrophysical Research Consortium for the Participating Institutions of the SDSS Collaboration, including the Brazilian Participation Group, the Carnegie Institution for Science, Carnegie Mellon University, Center for Astrophysics—Harvard & Smithsonian, the Chilean Participation Group, the French Participation Group, Instituto de Astrofísica de Canarias, Johns Hopkins University, Kavli Institute for the Physics and Mathematics of the Universe (IPMU)/University of Tokyo, the Korean Participation Group, Lawrence Berkeley National Laboratory, Leibniz Institut für Astrophysik Potsdam (AIP), Max-Planck-Institut für Astronomie (MPIA Heidelberg), Max-Planck-Institut für Astrophysik (MPA Garching), Max-Planck-Institut für Extraterrestrische Physik (MPE), National Astronomical Observatories of China, New Mexico State University, New York University, University of Notre Dame, Observatário Nacional/MCTI, The Ohio State University, Pennsylvania State University, Shanghai Astronomical Observatory, United Kingdom Participation Group, Universidad Nacional Autónoma de México, University of Arizona, University of Colorado Boulder, University of Oxford, University of Portsmouth, University of Utah, University of Virginia, University of Washington, University of Wisconsin, Vanderbilt University, and Yale University.

Funding for the Sloan Digital Sky Survey V has been provided by the Alfred P. Sloan Foundation, the Heising-Simons Foundation, the National Science Foundation, and the Participating Institutions. SDSS acknowledges support and resources from the Center for High-Performance Computing at the University of Utah. SDSS telescopes are located at Apache Point Observatory, funded by the Astrophysical Research Consortium and operated by New Mexico State University, and at Las Campanas Observatory, operated by the Carnegie Institution for Science. The SDSS website is www.sdss.org. SDSS is managed by the Astrophysical Research Consortium for the Participating Institutions of the SDSS Collaboration, including Caltech, The Carnegie Institution for Science, Chilean National Time Allocation Committee (CNTAC) ratified researchers, The Flatiron Institute, the Gotham Participation Group, Harvard University, Heidelberg University, The Johns Hopkins University, L'École polytechnique fédérale de Lausanne (EPFL), Leibniz-Institut für Astrophysik Potsdam (AIP), Max-Planck-Institut für Astronomie (MPIA Heidelberg), Max-Planck-Institut für Extraterrestrische Physik (MPE), Nanjing University, National Astronomical Observatories of China (NAOC), New Mexico State University, The Ohio State University, Pennsylvania State University, Smithsonian Astrophysical Observatory, Space Telescope Science Institute (STScI), the Stellar Astrophysics Participation Group, Universidad Nacional Autónoma de México, University of Arizona, University of Colorado Boulder, University of Illinois at Urbana-Champaign, University of Toronto, University of Utah, University of Virginia, Yale University, and Yunnan University.

This work has made use of data from the European Space Agency (ESA) mission Gaia (https://www.cosmos.esa.int/gaia), processed by the Gaia Data Processing and Analysis Consortium (DPAC; https://www.cosmos.esa.int/web/gaia/dpac/consortium). Funding for the DPAC has been provided by national institutions, in particular the institutions participating in the Gaia Multilateral Agreement.

This research made use of Astropy, a community-developed core Python package for Astronomy (Astropy Collaboration et al. 2018).

*Facilities:* Du Pont (APOGEE), Sloan (APOGEE), Gaia.

*Software:* BACCHUS (T. Masseron et al. 2016), Turbospectrum (R. Alvarez & B. Plez 1998; B. Plez 2012), Astropy (Astropy Collaboration et al. 2013, 2018, 2022), Numpy (C. R. Harris et al. 2020), Matplotlib (J. D. Hunter 2007), Scipy (P. Virtanen et al. 2020).

## Appendix A
## Comparison of the Effective Temperature

As discussed in Section 3.2, the effective temperatures adopted in this work are derived from the well-established photometric calibrations of J. I. González Hernández & P. Bonifacio (2009), using five color indices: $B - V$, $V - J$, $V - H$, $V - K_s$, and $J - K_s$. In this appendix, we provide a one-to-one comparison between our adopted $T_{\rm eff}$ scale and several alternative temperature estimates: the J. I. González Hernández & P. Bonifacio (2009) calibration using only the $J - K_s$ color, the APOGEE DR17 temperatures (Abdurro'uf et al. 2022), and the APOGEE DR19 temperatures (SDSS Collaboration et al. 2026a). Figures 6 and 7 present a comparison among the effective temperature scales used or considered in this work for the NGC 752 and Ruprecht 147 open clusters, respectively. These include the photometric temperatures derived from different color combinations, the raw DR17 Synspec and Turbospectrum estimates obtained directly from spectral fitting, the raw DR19 effective temperatures, and the calibrated DR19 effective temperatures. The diagonal panels show the temperature distributions for each scale, while the lower panels show the pairwise comparisons. In each comparison panel, the dashed line marks the one-to-one relation. We also report the Pearson correlation coefficient, the mean temperature difference, and the dispersion around this difference.

Overall, the different temperature scales are strongly correlated, with most comparisons yielding correlation coefficients close to unity. The photometric effective temperatures adopted in this work are generally consistent with the spectroscopic and calibrated APOGEE temperature scales, although small systematic offsets are present. These offsets are typically of order ∼50–150 K, depending on the comparison scale, and are comparable to the expected uncertainties in the temperature determinations. The typical effective temperature uncertainty is about 50–70 K, comparable to the marker sizes in the figure. The raw DR19 and DR17 Synspec effective temperatures agree most closely with our adopted photometric scale, whereas the calibrated DR19 temperatures and the $J - K_s$-based photometric effective temperatures show the largest offsets. We also note that the raw DR17 Synspec and

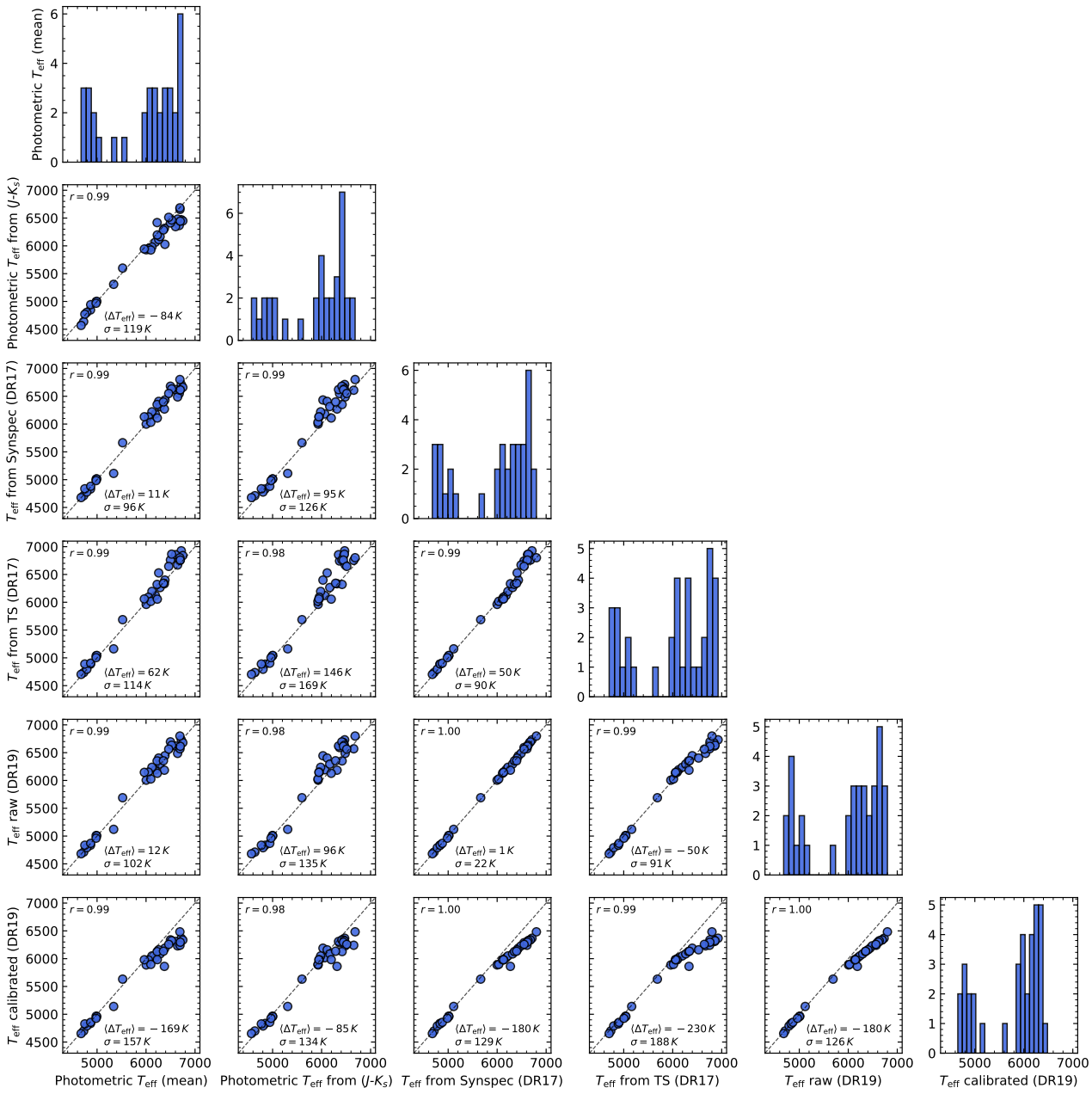


**Figure 6.** Comparison between the different effective temperature scales considered for NGC 752. The diagonal panels show the temperature distributions for each scale, while the lower panels show the pairwise comparisons. The temperature scales include the photometric $T_{\rm eff}$ adopted in this work, computed as the mean of five color calibrations; the photometric $T_{\rm eff}$ derived using only the $J - K_s$ color; the raw DR17 Synspec and Turbospectrum temperatures; and the raw and calibrated DR19 temperatures. The dashed line in each comparison panel indicates the one-to-one relation. Each panel also reports the Pearson correlation coefficient, $r$, the mean temperature difference, $\langle \Delta T_{\rm eff} \rangle$, and the corresponding dispersion, $\sigma$. Overall, the different temperature scales are strongly correlated, with small systematic offsets between them.

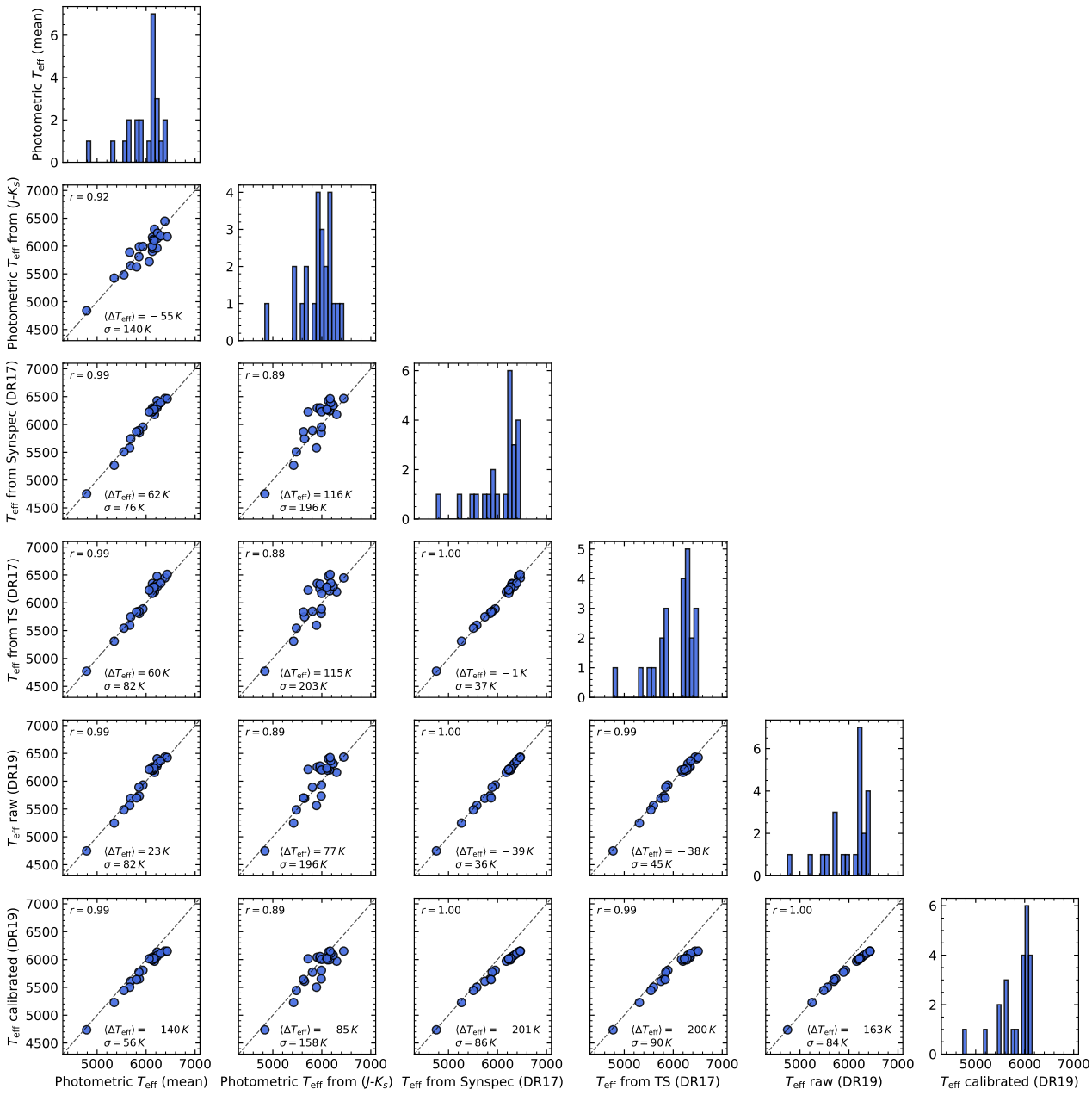


**Figure 7.** Same as Figure 6, but for Ruprecht 147.

raw DR19 temperatures yield virtually the same $T_{\rm eff}$ scale for NGC 752.

## Appendix B
## Comparison with Automated Abundance Pipelines

This appendix presents abundance comparisons between the values derived in this work and those available from APOGEE DR19, APOGEE DR17 Turbospectrum, and APOGEE DR17 Synspec. The presented figures are intended to quantify possible zero-point offsets and systematic differences among abundance scales and to verify whether the abundance trends discussed in the main text are specific to our analysis or also present in independent APOGEE determinations.

For all figures in this appendix, we show a corner-plot comparison of [X/H] abundances for NGC 752 (top panel) and Ruprecht (bottom panel) derived in this work and from different APOGEE abundance scales, as seen in Figure 8. The diagonal panels show the abundance distributions for each source: this work, APOGEE DR19, APOGEE DR17 Turbospectrum (TS), and APOGEE DR17 Synspec. The numbers in each diagonal panel indicate the mean abundance and standard deviation for the full sample and for each evolutionary stage studied. The value of $\Delta$(Diff $-$ CS) gives the abundance difference between the stars most likely to have atomic diffusion depletion and those at the cooler end of the main-sequence population studied in this work, and $S$ gives the significance of this difference in units of $\sigma$.

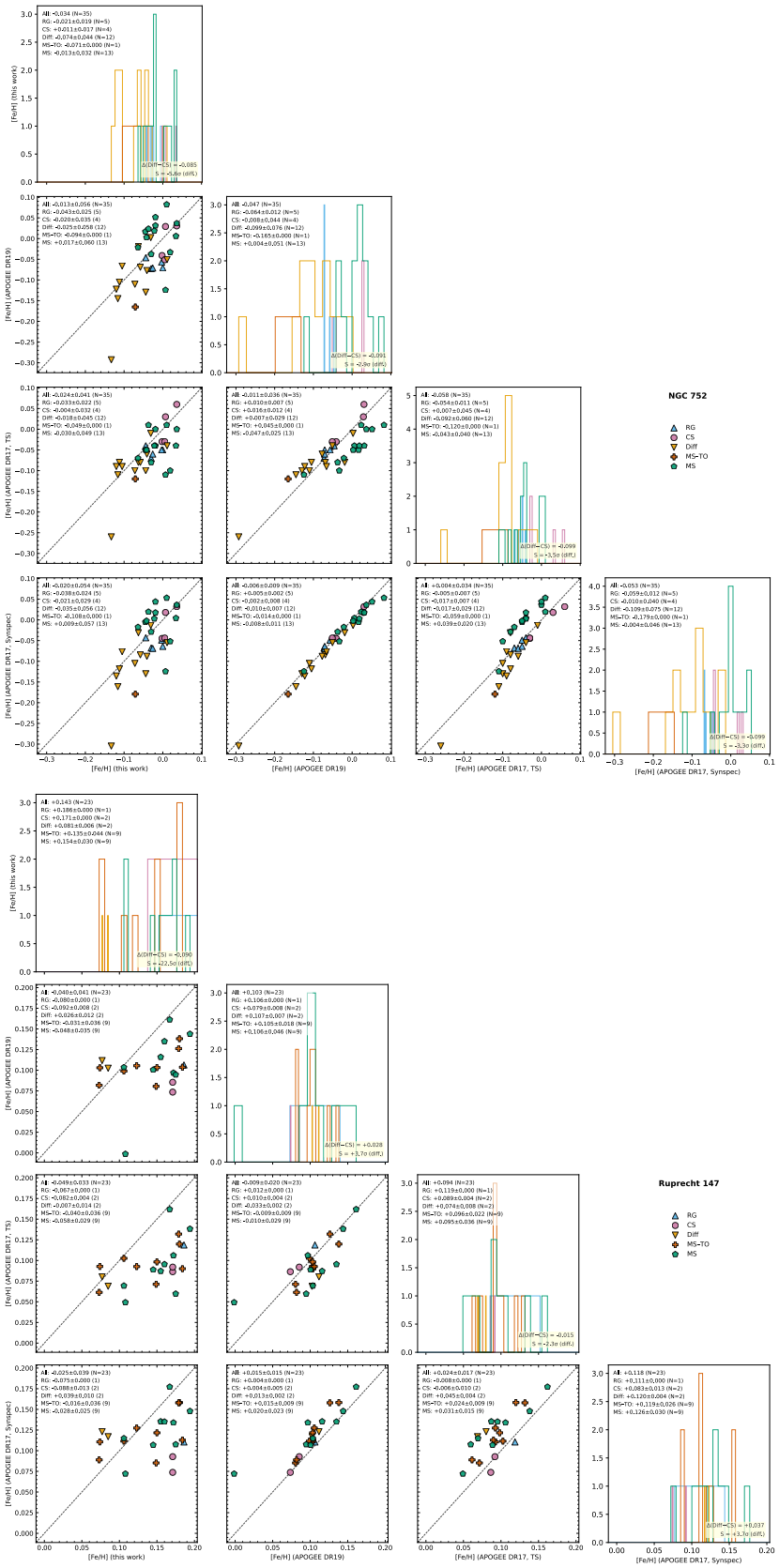


**Figure 8.** Top panel: abundance scale comparison for Fe in the NGC 752 open cluster. Bottom panel: same as the top panel, but for Ruprecht 147. The complete figure set (31 images) is available in the online journal.

(The complete figure set (32 images) is available in the online article.)

For each element, we quantify the abundance difference between the sample most likely to present an atomic diffusion signature (Diff) and the coolest stellar sample (CS) in what we assume to have the pristine cluster composition as

$$\Delta(\mathrm{Diff} - \mathrm{CS}) = \mu_{\mathrm{Diff}} - \mu_{\mathrm{CS}}, \tag{B1}$$

where $\mu_{\mathrm{Diff}}$ and $\mu_{\mathrm{CS}}$ represent the mean abundances. The uncertainty on this difference is estimated from the dispersion of each evolutionary group as

$$\sigma_{\Delta} = \left( \frac{\sigma^2_{\mathrm{TO}}}{N_{\mathrm{TO}}} + \frac{\sigma^2_{\mathrm{MS}}}{N_{\mathrm{MS}}} \right)^{1/2}, \tag{B2}$$

where $\sigma_{\mathrm{Diff}}$ and $\sigma_{\mathrm{CS}}$ are the abundance dispersions within the samples and $N_{\mathrm{Diff}}$ and $N_{\mathrm{CS}}$ are the corresponding number of stars. We then define the significance of the abundance offset as

$$S = \frac{\Delta(\mathrm{Diff} - \mathrm{CS})}{\sigma_{\Delta}}. \tag{B3}$$

Negative values of $\Delta(\mathrm{Diff} - \mathrm{CS})$ indicate that the Diff stars are depleted relative to the CS reference population. We consider abundance differences with $|S| > 1$ statistically significant (*likely* in the figures) and those with $|S| > 2$ as strong evidence for a depletion signature (*diff* in the figures).

The lower panels of this appendix figure show the pairwise abundance comparisons between different sources. The dashed line indicates the one-to-one relation, and the inset text gives the mean abundance offset, $\langle \Delta[\mathrm{Fe/H}] \rangle$, and standard deviation for all stars and for each evolutionary group. Symbols indicate the evolutionary stage: cyan upward-pointing triangles are red giants (RG), pink circles are the cooler main-sequence stars (CS), gold downward-pointing triangles are stars at the expected atomic diffusion dip (Diff), red plus signs are the stars close to the turnoff region (MS–TO), and the green pentagons are main-sequence stars with masses close to the Sun (MS).

## ORCID iDs

Diogo Souto https://orcid.org/0000-0002-7883-5425
Taylor Spoo https://orcid.org/0000-0003-4019-5167
Peter M. Frinchaboy https://orcid.org/0000-0002-0740-8346
Katia Cunha https://orcid.org/0000-0001-6476-0576
Jamie Tayar https://orcid.org/0000-0002-4818-7885
Alessa Ibrahim Wiggins https://orcid.org/0009-0008-0081-764X
Natalie Myers https://orcid.org/0000-0001-9738-4829

## References

Abdurro'uf, Accetta, K., Aerts, C., et al. 2022, ApJS, 259, 35
Agüeros, M. A., Curtis, J. L., & Núñez, A. 2025, ApJ, 993, 144
Alvarez, R., & Plez, B. 1998, A&A, 330, 1109
Astropy Collaboration, Price-Whelan, A. M., Lim, P. L., et al. 2022, ApJ, 935, 167
Astropy Collaboration, Price-Whelan, A. M., Sipőcz, B. M., et al. 2018, AJ, 156, 123
Astropy Collaboration, Robitaille, T. P., Tollerud, E. J., et al. 2013, A&A, 558, A33
Beaton, R. L., Oelkers, R. J., Hayes, C. R., et al. 2021, AJ, 162, 302
Beeson, K. L., Kos, J., de Grijs, R., et al. 2024, MNRAS, 529, 2483
Bertelli Motta, C., Pasquali, A., Richer, J., et al. 2018, MNRAS, 478, 425
Blanton, M. R., Bershady, M. A., Abolfathi, B., et al. 2017, AJ, 154, 28
Boesgaard, A. M., Deliyannis, C. P., Stephens, A., & King, J. R. 1998, ApJ, 493, 206
Bowen, I. S., & Vaughan, A. H. J. 1973, ApOpt, 12, 1430
Bragaglia, A., Fu, X., Mucciarelli, A., Andreuzzi, G., & Donati, P. 2018, A&A, 619, A176
Cantat-Gaudin, T., Anders, F., Castro-Ginard, A., et al. 2020, A&A, 640, A1
Carrera, R., Bragaglia, A., Cantat-Gaudin, T., et al. 2019, A&A, 623, A80
Casagrande, L., Silva Aguirre, V., Schlesinger, K. J., et al. 2016, MNRAS, 455, 987
Chapman, S. 1917a, MNRAS, 77, 539
Chapman, S. 1917b, MNRAS, 77, 540
Choi, J., Dotter, A., Conroy, C., et al. 2016, ApJ, 823, 102
Cunha, K., Smith, V. V., Johnson, J. A., et al. 2015, ApJL, 798, L41
Cutri, R. M., Skrutskie, M. F., van Dyk, S., et al. 2003, IRSA 2MASS All-Sky Point Source Catalog, NASA/IPAC Infrared Science Archive
Donor, J., Frinchaboy, P. M., Cunha, K., et al. 2018, AJ, 156, 142
Donor, J., Frinchaboy, P. M., Cunha, K., et al. 2020, AJ, 159, 199
Dotter, A. 2016, ApJS, 222, 8
Dotter, A., Conroy, C., Cargile, P., & Asplund, M. 2017, ApJ, 840, 99
Eisenstein, D. J., Weinberg, D. H., Agol, E., et al. 2011, AJ, 142, 72
Freeman, K., & Bland-Hawthorn, J. 2002, ARA&A, 40, 487
Frinchaboy, P. M., Thompson, B., Jackson, K. M., et al. 2013, ApJL, 777, L1
Gao, X., Lind, K., Amarsi, A. M., et al. 2018, MNRAS, 481, 2666
García Pérez, A. E., Allende Prieto, C., Holtzman, J. A., et al. 2016, AJ, 151, 144
Gilmore, G., Randich, S., Asplund, M., et al. 2012, Msngr, 147, 25
González Hernández, J. I., & Bonifacio, P. 2009, A&A, 497, 497
Grilo, V., Souto, D., Cunha, K., et al. 2024, MNRAS, 534, 3005
Gruyters, P., Korn, A. J., Richard, O., et al. 2013, A&A, 555, A31
Gruyters, P., Nordlander, T., & Korn, A. J. 2014, A&A, 567, A72
Gunn, J. E., Siegmund, W. A., Mannery, E. J., et al. 2006, AJ, 131, 2332
Gustafsson, B., Edvardsson, B., Eriksson, K., et al. 2008, A&A, 486, 951
Harris, C. R., Millman, K. J., van der Walt, S. J., et al. 2020, Natur, 585, 357
Hayden, M. R., Sharma, S., Bland-Hawthorn, J., et al. 2022, MNRAS, 517, 5325
Holtzman, J. A., Hasselquist, S., Shetrone, M., et al. 2018, AJ, 156, 125
Hunter, J. D. 2007, CSE, 9, 90
Jönsson, H., Holtzman, J. A., Allende Prieto, C., et al. 2020, AJ, 160, 120
Karakas, A. I., & Lattanzio, J. C. 2014, PASA, 31, e030
King, J. R., Stephens, A., Boesgaard, A. M., & Deliyannis, C. 1998, AJ, 115, 666
Korn, A. J., Grundahl, F., Richard, O., et al. 2006, Natur, 442, 657
Korn, A. J., Grundahl, F., Richard, O., et al. 2007, ApJ, 671, 402
Lagarde, N., Decressin, T., Charbonnel, C., et al. 2012, A&A, 543, A108
Liu, F., Asplund, M., Yong, D., et al. 2019, A&A, 627, A117
Loaiza-Tacuri, V., Cunha, K., Souto, D., et al. 2023, MNRAS, 526, 2378
Lum, M. G., & Boesgaard, A. M. 2019, ApJ, 878, 99
Magrini, L., Viscasillas Vázquez, C., Spina, L., et al. 2023, A&A, 669, A119
Majewski, S. R., Schiavon, R. P., Frinchaboy, P. M., et al. 2017, AJ, 154, 94
Martell, S. L., Sharma, S., Buder, S., et al. 2017, MNRAS, 465, 3203
Masseron, T., Merle, T., & Hawkins, K. 2016, BACCHUS: Brussels Automatic Code for Characterizing High accUracy Spectra, Astrophysics Source Code Library, ascl:1605.004
Michaud, G., Alecian, G., & Richer, J. 2015, Atomic Diffusion in Stars, Astronomy and Astrophysics Library (Springer)
Michaud, G., Richard, O., Richer, J., & VandenBerg, D. A. 2004, ApJ, 606, 452
Myers, N., Donor, J., Spoo, T., et al. 2022, AJ, 164, 85
Nordlander, T., Gruyters, P., Richard, O., & Korn, A. J. 2024, MNRAS, 527, 12120
Önehag, A., Gustafsson, B., & Korn, A. 2014, A&A, 562, A102
Osorio, Y., Allende Prieto, C., Hubeny, I., Mészáros, S., & Shetrone, M. 2020, A&A, 637, A80
Otto, J. M., Frinchaboy, P. M., Myers, N. R., et al. 2026, AJ, 171, 91
Paxton, B., Bildsten, L., Dotter, A., et al. 2011, ApJS, 192, 3
Paxton, B., Cantiello, M., Arras, P., et al. 2013, ApJS, 208, 4
Paxton, B., Marchant, P., Schwab, J., et al. 2015, ApJS, 220, 15
Plez, B. 2012, Turbospectrum: Code for spectral synthesis, Astrophysics Source Code Library, ascl:1205.004
Proffitt, C. R., & Michaud, G. 1991, ApJ, 380, 238
Prša, A., Harmanec, P., Torres, G., et al. 2016, AJ, 152, 41
Randich, S., Tognelli, E., Jackson, R., et al. 2018, A&A, 612, A99
Reddy, A. B. S., Giridhar, S., & Lambert, D. L. 2012, MNRAS, 419, 1350
Richer, J., Michaud, G., Rogers, F., et al. 1998, ApJ, 492, 833
Santana, F. A., Beaton, R. L., Covey, K. R., et al. 2021, AJ, 162, 303

Sarajedini, A., Dotter, A., & Kirkpatrick, A. 2009, ApJ, 698, 1872
SDSS Collaboration, Adamane Pallathadka, G., Aghakhanloo, M., et al. 2026a, ApJS, 285, 9
SDSS Collaboration, Aghakhanloo, M., Aird, J., et al. 2026b, ApJS, 285, 9
Semenova, E., Bergemann, M., Deal, M., et al. 2020, A&A, 643, A164
Sinha, A., Zasowski, G., Frinchaboy, P., et al. 2024, ApJ, 975, 89
Smith, V. V., Cunha, K., Shetrone, M. D., et al. 2013, ApJ, 765, 16
Soderblom, D. R. 2010, ARA&A, 48, 581
Souto, D., Allende Prieto, C., Cunha, K., et al. 2019, ApJ, 874, 97
Souto, D., Cunha, K., García-Hernández, D. A., et al. 2017, ApJ, 835, 239
Souto, D., Cunha, K., & Smith, V. V. 2021, ApJ, 917, 11
Souto, D., Cunha, K., Smith, V., et al. 2016, ApJ, 830, 35
Souto, D., Cunha, K., Smith, V. V., et al. 2018a, ApJ, 857, 14
Souto, D., Pascucci, I., Cunha, K., & Kanodia, S. 2026, ApJL, 1001, L28
Souto, D., Unterborn, C. T., Smith, V. V., et al. 2018b, ApJL, 860, L15
Thoul, A. A., Bahcall, J. N., & Loeb, A. 1994, ApJ, 421, 828
Torres, G., Andersen, J., & Giménez, A. 2010, A&ARv, 18, 67
VandenBerg, D. A., Bergbusch, P. A., Dotter, A., et al. 2012, ApJ, 755, 15
VandenBerg, D. A., Richard, O., Michaud, G., & Richer, J. 2002, ApJ, 571, 487
Virtanen, P., Gommers, R., Oliphant, T. E., et al. 2020, NaMet, 17, 261
Wilson, J. C., Hearty, F. R., Skrutskie, M. F., et al. 2019, PASP, 131, 055001
Xiang, M., & Rix, H.-W. 2022, Natur, 603, 599
Zacharias, N., Finch, C. T., Girard, T. M., et al. 2013, AJ, 145, 44
Zasowski, G., Cohen, R. E., Chojnowski, S. D., et al. 2017, AJ, 154, 198
Zasowski, G., Johnson, J. A., Frinchaboy, P. M., et al. 2013, AJ, 146, 81